

Combined carbon, hydrogen, and clumped isotope fractionations reveal differential reversibility of hydrogenotrophic methanogenesis in laboratory cultures

Jeemin H. Rhim[a,1,*] and Shuhei Ono[a]

[a] *Department of Earth, Atmospheric and Planetary Sciences, Massachusetts Institute of Technology, Cambridge, MA 02139, USA. jrhim@alum.mit.edu (J. H. Rhim), sono@mit.edu (S. Ono)*
[1] *Present address: Department of Earth Sciences, Dartmouth College, Hanover, NH 03755, USA*
[*] *Corresponding author: jrhim@alum.mit.edu*

A manuscript prepared for submission to *Geochimica Cosmochimica Acta*

Abstract

Stable isotope analysis has been widely used to aid the source identification of methane. However, the isotopic ($^{13}C/^{12}C$ and D/H) and isotopologue ($^{13}CH_3D$ and $^{12}CH_2D_2$) signatures of microbial methane in natural environments are often different from those in laboratory cultures in which methanogens are typically grown under optimal conditions. Growth phase and hydrogen (H_2) concentration have been proposed as factors controlling the isotopic compositions of methane produced via hydrogenotrophic methanogenesis, but their effects on the relationship among carbon, hydrogen and doubly-substituted "clumped" isotopologue systems have not been assessed in a quantitative framework. Here we experimentally investigate the bulk ($\delta^{13}C$ and δD) and clumped ($\Delta^{13}CH_3D$) isotopologue compositions of methane produced by hyperthermophilic hydrogenotrophic (CO_2-reducing) methanogens using batch and fed-batch systems at different growth phases and H_2 mixing ratios (*Methanocaldococcus bathoardescens* at 82 or 60 °C and on 80 or 25% H_2; *Methanothermobacter thermautotrophicus* ΔH at 65 °C and on 20, 5 or 1.6% H_2). We observed a large range (18 to 63‰) of carbon isotope fractionations, with larger values observed during later growth phase, consistent with previous observations. In contrast, hydrogen isotope fractionations remained relatively constant at –317 ± 25‰. Linear growth was observed for experiments with *M. bathoardescens*, suggesting that dissolution of gaseous H_2 into liquid media became the rate limit as cell density increased. Accordingly, the low (and undersaturated) dissolved H_2 concentrations can explain the increased carbon isotope fractionations during the later growth phase. The δD and $\Delta^{13}CH_3D$ values indicated departure from equilibrium throughout experiments. As the cell density increased and dissolved H_2 decreased, $\Delta^{13}CH_3D$ decreased (further departure from equilibrium), contrary to expectations from previous models. Our isotopologue flow network model reproduced the observed trends when the last H-addition step is less reversible relative to the first three H-addition steps (up to CH_3-CoM). In this differential reversibility model, carbon, hydrogen and clumped isotopologue fractionations are largely controlled by the reversibility of the first three H-addition steps under high H_2 concentrations; the last H-addition step becomes important under low H_2. The magnitude of depletion and decreasing trend in $\Delta^{13}CH_3D$ values were reproduced when a large (≥6‰) secondary clumped kinetic isotope

effect was considered in the model. This study highlights the advantage of combined bulk and clumped isotope analyses and the importance of physiological factors (growth phase) and energy availability (dissolved H_2 concentration) when using isotope analyses to better understand methanogenic metabolisms and methane cycling processes.

1 Introduction

Methane (CH_4) is an important energy source, a potent greenhouse gas as well as a potential biosignature in subsurface and extraterrestrial environments. Stable carbon ($\delta^{13}C$) and hydrogen (δD) isotope ratios have been extensively used to apportion the relative contributions of different methanogenic pathways, e.g., acetoclastic *vs*. hydrogenotrophic methanogenesis (Welhan and Lupton, 1987; Whiticar, 1990; Sherwood Lollar et al., 2002; Flores et al., 2008; Sherwood Lollar et al., 2008; Pohlman et al., 2009; Baldassare et al., 2014). More recently, technological advances have allowed the precise measurements of the abundance of multiply-substituted or "clumped" isotopologues of methane (e.g., $^{13}CH_3D$ and $^{12}CH_2D_2$; Ono et al., 2014; Stolper et al., 2014; Young et al., 2016; Gonzalez et al., 2019). Methane clumped isotopologue abundance has in some cases served as an isotopic geothermometer and provided temperature estimates that are consistent with environmental temperatures (e.g., Stolper et al., 2015; Wang et al., 2015; Young et al., 2017).

While both bulk and clumped isotopic compositions of methane can help identify the source(s) of methane, some factors complicate the interpretation of the isotopic signatures. For example, overlapping isotopic signatures in $\delta^{13}C$ and δD often lead to ambiguous source identifications (e.g., Schoell, 1988; Whiticar, 1990, 1999; Pohlman et al., 2009; Etiope and Sherwood Lollar, 2013), and some microbial methane samples from surface environments (e.g., freshwater lakes, swamps, and cow rumen) have yielded unreasonably high temperature estimates for clumped isotopologue equilibrium (e.g., Stolper et al., 2015; Wang et al., 2015; Douglas et al., 2017; Young et al., 2017). In particular, there are significant discrepancies between the bulk and clumped isotopic signatures observed in natural samples of microbial methane and those produced by laboratory cultures that presumably use the same metabolic pathway (Stolper et al., 2015; Wang et al., 2015; Douglas et al., 2016; Okumura et al., 2016; Young et al., 2017; Gruen et al., 2018; Giunta et al., 2019; Douglas et al., 2020). In general, the $\delta^{13}C$ and δD values of microbial methane in marine environments, where hydrogenotrophic methanogenesis is thought to be a primary methanogenic pathway, tend to indicate isotopic equilibrium with CO_2 and H_2O. In contrast, the $\delta^{13}C$ and δD values observed in laboratory cultures often indicate kinetic isotope effect (i.e., a departure from equilibrium). Similarly, the $\Delta^{13}CH_3D$ values, representing the relative abundance of $^{13}CH_3D$ clumped isotopologues, measured from microbial methane in marine and deep subsurface sediments indicate internal isotopic equilibrium whereas those from pure cultures carry strong kinetic isotope signatures (Stolper et al., 2015; Wang et al., 2015; Douglas et al., 2017; Young et al., 2017; Gruen et al., 2018). It has been suggested that anaerobic oxidation of methane (AOM) is required for isotopic equilibrium of marine microbial methane. Recent studies have reported observations consistent with this hypothesis (Ash et al., 2019; Giunta et al., 2019; Zhang et al., 2021). However, it remains unclear whether microbial methanogenesis alone can produce near-equilibrium isotope signatures without the external oxidative process (e.g., Okumura et al., 2016; Turner et al., 2021; Gropp et al., 2022; Ono et al., 2022).

Previous studies that investigated the factors controlling isotope fractionation during microbial methanogenesis shed some light on the cause of the observed discrepancy. Multiple studies have investigated the changes in the carbon isotope fractionation factor ($^{13}\alpha$) during hydrogenotrophic methanogenesis and have identified growth phase and/or hydrogen partial pressure (pH_2) as important controlling factors (Games and Hayes, 1978; Fuchs et al., 1979a; Belyaev et al., 1983; Balabane et al., 1987; Krzycki et al., 1987; Botz et al., 1996; Valentine et al., 2004; Penning et al., 2005; Londry et al., 2008; Yoshioka et al., 2008; Hattori et al., 2012; Okumura et al., 2016; Topçuoğlu et al., 2019; Nguyen et al., 2020). In general, carbon isotope fractionation increases (lower $^{13}\alpha$ values) at low pH_2 such that the apparent magnitude of fractionation is close to that expected at CH_4-CO_2 equilibrium. These observations corroborate the differential reversibility hypothesis, which predicts that the variation in carbon isotope fractionation is a result of the changes in reversibility in the enzymatic steps of the hydrogenotrophic methanogenesis pathway (Valentine et al., 2004).

The effect of pH_2 on hydrogen isotope fractionation has been investigated by comparing pure cultures grown on high concentrations of H_2 against cocultures containing hydrogenotrophic methanogens and syntrophic heterotrophic bacteria (e.g., *Syntropothermus lipocalidus* str. TGB-C1 and *Methenothermobacter thermautotrophicus* str. ΔH) (Yoshioka et al., 2008; Hattori et al., 2012; Okumura et al., 2016). Cocultures provide a means to create relatively low H_2 conditions (e.g., 6.8 to 64.9 Pa; Okumura et al., 2016) compared to high pH_2 conditions (>10^5 Pa) often used for pure cultures grown on H_2. So far, to the best of our knowledge, no experiment has observed the magnitude of hydrogen isotope fractionation expected at CH_4-H_2O equilibrium (*ca*. –178‰ at 25 °C; Horita and Wesolowski, 1994; Gropp, Iron and Halevy, 2021) that is often observed in natural samples of microbial methane in marine environments. If the differential reversibility hypothesis can be applied to hydrogen isotope system, higher reversibility and near-equilibrium hydrogen isotope fractionation are expected at lower H_2 environments. This would suggest that the H_2 concentrations tested in experiments so far were not low enough to produce near-equilibrium hydrogen isotope signatures.

Laboratory experiments investigating methane clumped isotope fractionation during hydrogenotrophic methanogenesis have only been conducted in batch cultures under high pH_2

conditions (e.g., Stolper et al., 2015; Wang et al., 2015; Young et al., 2017; Gruen et al., 2018; Giunta et al., 2019). Isotope models relating the dissolved H_2 concentration and $\Delta^{13}CH_3D$ values have been proposed and predict changes in $\Delta^{13}CH_3D$ values toward equilibrium (i.e., increase in $\Delta^{13}CH_3D$ values toward 6‰ at 25 °C) at low H_2 concentrations (e.g., Stolper et al., 2015; Wang et al., 2015), consistent with the overall concept of the differential reversibility hypothesis. However, direct investigations of $\Delta^{13}CH_3D$ values produced at different growth phases or H_2 concentrations are needed to validate whether the differential reversibility model can be applied to clumped isotopologue systematics.

In this study, we cultured two different species of methanogens, *Methanocaldococcus bathoardescens* and *Methanothermobacter thermautotrophicus* str. ΔH, in batch and fed-batch systems under a pH_2 range from 1.6 kPa to 80 kPa and simultaneously measured $\delta^{13}C$ and δD of CO_2 and H_2O (carbon and hydrogen sources for CH_4) as well as the $\delta^{13}C$, δD and $\Delta^{13}CH_3D$ of the product (CH_4). We present isotopologue flow network model results along with the estimated dissolved H_2 concentrations and measured isotopologue ratios to explain the observed fractionation trends by the effects of differential reversibility at the last H-addition step. We propose the $\delta^{13}C$, δD and $\Delta^{13}CH_3D$ trajectories expected for a wide range of dissolved H_2 concentrations encompassing both natural environments and experimental conditions (10^{-9} to 10^{-2} M H_2) that can be applied for future investigations of these isotope signatures for source identifications of methane.

2 Materials and Methods

2.1 Organisms

Cultures of *Methanocaldococcus bathoardescens* were provided by James F. Holden (University of Massachusetts, Amherst). Culture medium for *M. bathoardescens* was prepared following the "282 mod" recipe (Ver Eecke *et al.*, 2012) containing (L^{-1}): 0.34 g KCl, 4.00 g $MgCl_2 \cdot 6H_2O$, 0.14 g KH_2PO_4, 3.45 g $MgSO_4 \cdot 7H_2O$, 18 g NaCl, 0.25 g NH_4Cl, 0.14 g $CaCl_2 \cdot 2H_2O$, 2.0 mL $Fe(NH_4)_2(SO_4)_2 \cdot 6H_2O$ (0.1% w/v), 10.0 mL trace element solution SL-10 (DSMZ 320), 5.00 g $NaHCO_3$, 10.0 mL vitamins solution (DSMZ 141). Resazurin was omitted, and 2 mM cysteine and 1 mM sulfide were used as reducing agents instead of dithiothreitol.

Methanothermobacter thermautotrophicus str ΔH (DSM 1053) was purchased from the German Collection of Microorganisms and Cell Cultures (DSMZ, Braunschweig, Germany). The seed culture was transferred to and maintained in mineral medium modified from DSMZ 1523 containing (L^{-1}): 0.50 g KH_2PO_4, 0.40 g $MgSO_4 \cdot 7H_2O$, 0.40 g NaCl, 0.40 g NH_4Cl, 0.05 g $CaCl_2 \cdot 2H_2O$, 1.00 mL trace element solution SL-10 (DSMZ 320), 4.00 g $NaHCO_3$, 1.00 mL vitamins solution (DSMZ 503). The medium was reduced with 1 mM sulfide.

2.2 Culture conditions

Table 1 summarizes the conditions for culture experiments conducted in this study. *M. bathoardescens* was grown at 82 or 60 °C and on 80 or 25% H_2, and *M. thermautotrophicus* ΔH was grown at 65 °C and on 20, 5 or 1.6% H_2.

2.2.1 Batch cultures

M. bathoardescens batch culture series was prepared in 100 mL of "282mod" medium described above in 200 mL bottles with 2 bars absolute pressure of H_2/CO_2 (80:20). Each bottle was inoculated with 2% (v/v) of pre-culture in exponential growth phase. Cultures were incubated at 82 °C. At given timepoints, culture headspace was sampled for gas chromatography and $\delta^{13}C_{CO2}$ analysis. Medium was sampled for cell counts with a counting chamber (CTL-HEMM-GLDR, LW Scientific; depth = 0.1 mm) and phase-contrast light microscope. Immediately after sampling, the entire remaining culture was sacrificed by adding 5 mL of 1 M sodium hydroxide. The headspace of a killed culture was used for methane purification and subsequent isotopologue analysis.

2.2.2 Fed-batch cultures

All fed-batch culturing experiments were carried out using a 2-L glass bioreactor (Ace Glass) equipped with a fritted gas dispersion tube (Ace Glass), pH meter (ML-05990-40; Cole-Parmer), temperature monitor/controller, liquid sampling port and a condenser leading to the gas outlet (Figure 1). Both the culturing apparatus and 1.7 L of medium were sterilized by autoclaving at 121 °C for 20 minutes. A set of mass flow controllers was used to control the flow rates of H_2, CO_2 and He (or N_2) to achieve desired mixing ratios of H_2, xH_2, (80, 25, 20, 5 and 1.6%) in the influent gas (Table 1). A column filled with copper was placed between the gas tanks and the reactor and heated to 450 °C to remove trace amounts of oxygen in the incoming gas mixture (Wolfe, 2011). After the reactor was heated to desired temperatures (82, 65 or 60 °C), vitamin solution was added and the pH was adjusted to 6.0 and 7.0 (for *M. bathoardescens* and *M. thermautotrophicus*, respectively) while bubbling with the gas mixture (20% CO_2). Cysteine (2 mM) and sulfide (2 mM) or cysteine (2 mM) and titanium citrate (0.1 mM) were added as reducing agents before adding a 2% (v/v) of inoculum. Effluent gas from the reactor was passed through a condenser (12 °C) which is followed by an additional column filled with $CaCl_2$ for water removal, and directly connected to an on-line gas chromatography system or a gas sampling bag (Cali-5-Bond™, Calibrated Instruments, Inc., McHenry, MD, USA) (Figure 1). Each gas sample was collected for at least 5 minutes (typically between 5 and 12 minutes) such that the sampling interval is comparable to or longer than the residence time of methane in the reactor headspace (~5 minutes).

2.3 Analytical procedures

2.3.1 Gas chromatography

Mixing ratios of headspace gases were measured using a gas chromatograph (GC-2014, Shimadzu, Columbia, MD, USA), equipped with a packed column (Carboxen-1000, 5' by 1/8", Supelco, Bellefonte, PA, USA) with argon carrier gas at 140 °C. A thermal conductivity and a methanizer-flame ionization detector were used to quantify the mixing ratios of H_2, N_2, CH_4 and CO_2. The following compositions of commercial and in-house standard gases were used for calibration: 7% CO, 15% CO_2, 4% O_2, 4.5% CH_4 balanced in N_2 (Supelco; P/N 501743); 4% CH_4, 20% CO_2, 2% CO balanced in N_2 (MESA International Technologies, Inc.); 80% H_2, 20% CO_2 (Airgas). The accuracy of GC analyses was ±5% of measured values. Headspace samples from experiments B.82 and F.82.80 were analyzed via manual syringe injection, and all other experiments were measured on-line GC using a gas sampling valve with a 500µL injection loop (VC-SL500CW, VICI Valco, Houston, TX, USA) (Figure 1).

2.3.2 $\delta^{13}C_{CO2}$ analysis

The carbon isotopic composition of headspace CO_2 ($\delta^{13}C_{CO2}$) was measured using a dual-inlet isotope-ratio mass spectrometer (IRMS; MAT 253, Thermo-Fisher). CO_2 from subsamples of the headspace gas collected from serum bottles (batch cultures) or at the exhaust (fed-batch cultures) was purified by cryogenically separating water and CO_2 from H_2, N_2 and CH_4 into a cold trap at –196 °C and warming up the trap to –80 °C and freezing the eluted CO_2 in a sample vial. The isotope ratios are normalized against VPDB using two CO_2 references (OzTech Trading Corporation; $\delta^{13}C$ = –40.49‰ and –10.38‰ VPDB). Typical analytical precision for $\delta^{13}C$ analysis is ±0.2‰.

2.3.3 δD_{H2O} analysis

The hydrogen isotopic composition of media water (δD_{H2O}) was measured using two different methods. For Experiments F.82.80 and F.60.80, δD_{H2O} was measured using a dual-inlet IRMS. Water samples were reduced with zinc following a previously described method (Coleman et al., 1982). The isotope ratios are normalized against VSMOW using H_2 references (OzTech Trading Corporation; δD = –124.83‰ and –49.52‰ VSMOW). For Experiments F.82.25, F.65.20 and F.65.5, δD_{H2O} was measured using cavity ring-down spectrometry (L-1102i WS-CRDS, Picarro, Sunnyvale, CA, USA) at the University of Massachusetts Amherst. Samples were vaporized at 110 °C. International reference standards (IAEA, Vienna, Austria) were used to calibrate the instrument to the VSMOW-VSLAP scale and working standards were used with each analytical run. Long-term averages of internal laboratory standard analytical results yield an instrumental precision of 0.5‰.

2.3.4 Methane isotopologue analysis

Methane samples were purified following the preparative GC method described by Wang et al. (2015). For batch culture experiment (B.82), the headspace of each killed serum bottle was attached to the preparatory GC setup, and a stream of helium (carrier gas for GC) replaced the headspace more than three times its volume. For fed-batch experiments, multi-layer foil sampling bags (Cali-5-Bond™, Calibrated Instruments, Inc., McHenry, MD, USA) used to collect downstream headspace gas at the exhaust were directly connected to the sample preparation system. The relative abundances of methane isotopologues $^{12}CH_4$, $^{13}CH_4$, $^{12}CH_3D$ and $^{13}CH_3D$ were measured using a tunable infrared laser direct absorption spectroscopy (TILDAS) described previously (Ono et al., 2014; Wang et al., 2015). Values of $\delta^{13}C$ and δD of methane analyzed via TILDAS were calibrated via measurements of natural gas standards NGS-1 and NGS-3 (Wang et al., 2015) using the reference values reported in Hut (1987). To correct for the nonlinearity in the spectroscopic analysis described by Ono et al. (2014), methane samples with a range of δD values (*ca.* –400‰ to +200‰ vs. VSMOW) were thermally equilibrated over platinum catalyst at 250 °C for at least two weeks and measured on TILDAS along with samples.

2.3.5 Isotope notation and calculation of isotope fractionation factors

Bulk isotope values are reported using standard delta notation:

$$\delta^{13}C = \frac{(^{13}C/^{12}C)_{sample}}{(^{13}C/^{12}C)_{VPDB}} - 1 \qquad \text{(Eqn. 1)}$$

$$\delta D = \frac{(D/H)_{sample}}{(D/H)_{VSMOW}} - 1 \qquad \text{(Eqn. 2)}$$

where VPDB and VSMOW are Vienna Pee Dee Belemnite and Vienna Standard Mean Ocean Water, respectively. The factor of 1000 was omitted from (Eqn. 1) and (Eqn. 2), following the IUPAC recommendations (Coplen, 2011). Natural gas samples with published $\delta^{13}C$ and δD values (NGS-1 and NGS-3) were used for the calibration of $\delta^{13}C$ and δD values of methane analyzed via TILDAS (Wang et al., 2015). Experimental samples were considered to contain methane isotopologues at or sufficiently close to their natural abundances, hence the following approximations are valid within analytical uncertainty: $^{13}C/^{12}C \approx [^{13}CH_4]/[^{12}CH_4]$ and $D/H \approx ¼ [^{12}CH_3D]/[^{12}CH_4]$. The abundance of $^{13}CH_3D$ clumped isotopologue is reported as $\Delta^{13}CH_3D$, a metric representing the deviation of the abundance of $^{13}CH_3D$ from a random distribution of isotopes among isotopologues $^{12}CH_4$, $^{13}CH_4$, $^{12}CH_3D$ and $^{13}CH_3D$ (Ono et al., 2014; Wang et al., 2015):

$$\Delta^{13}CH_3D = \frac{[^{13}CH_3D][^{12}CH_4]}{[^{13}CH_4][^{12}CH_3D]} - 1 \qquad \text{(Eqn. 3)}$$

The value of $\Delta^{13}CH_3D$ was calibrated by equilibrating methane at 250 °C using Pt catalyst (Ono et al., 2014).

The isotope fractionation factor (α) is defined as the ratio of relative abundances of isotopes between a substrate and its product. For a batch experiment (B.82), isotope fractionation factors are calculated assuming an irreversible closed system isotope effect, based on the conventional Rayleigh equation (Mariotti et al., 1981). For the reduction of CO_2 to CH_4:

$$(^{13}\alpha - 1) \cdot \ln f = \ln \frac{\delta^{13}C + 1}{\delta^{13}C_0 + 1} \qquad \text{(Eqn. 4)}$$

where f is the fraction of CO_2 remaining; $^{13}\alpha$ is the kinetic isotope fractionation factor for $^{13}C/^{12}C$; and $\delta^{13}C$ and $\delta^{13}C_0$ are the isotopic compositions of CO_2, with the subscript '0' indicating the initial time point (t=0).

The bulk isotope fractionation factors for fed-batch experiments (F.82.80, F.60.80, F.82.25, F.65.20 and F.65.5) were calculated as follows:

$$^{13}\alpha_{CH4/CO2} = \frac{\delta^{13}C_{CH4} + 1}{\delta^{13}C_{CO2} + 1} \qquad \text{(Eqn. 5)}$$

$$^{2}\alpha_{CH4/H2O} = \frac{\delta D_{CH4} + 1}{\delta D_{H2O} + 1} \qquad \text{(Eqn. 6)}$$

The equilibrium fractionation factors for carbon ($^{13}\alpha_{eq}$; Horita, 2001), hydrogen ($^{2}\alpha_{eq}$; Horibe and Craig, 1995) and clumped ($\Delta^{13}CH_3D_{eq}$; Ono et al., 2014) isotope systems were calculated based on experimental and/or theoretical calibrations.

The clumped isotopologue fractionation factor $^{13}CH_3D$ relative to $^{12}CH_4$ ($^{13,2}\alpha$) can closely approximate the product of $^{13}\alpha$ and $^{2}\alpha$, following the rule of geometric mean (Bigeleisen, 1955). The deviations from the rule is quantified by the "gamma-factor" ($^{13,2}\alpha = \gamma\ ^{13}\alpha \cdot {}^{2}\alpha$) as defined by Wang et al. (2016). For example, $\gamma = 1$when there is no clumped isotopologue effect.

2.3.6 Data processing

Methanogenesis reaction,

$$CO_{2(g)} + 4\ H_{2(g)} \rightarrow CH_{4(g)} + 2\ H_2O_{(l)} \qquad \text{(Eqn. 7)}$$

consumes 5 molecules of gas and produce 1 molecule of gas and water that is mostly in liquid phase. Because of this decrease in volume, the flow rate of effluent gas (Q_{out}) during fed-batch experiments does not equal to the flow rate of the influent gas (Q_{in}: 200 mL/min) and can be lower by up to 25% for our experimental conditions. Based on the stoichiometry of the reaction (Eqn. 7), the flow rate of effluent gas was calculated from the mixing ratios of H_2 and CH_4:

$$Q_{out} = \frac{x_{H2}^{in}}{4x_{CH4}^{out} + x_{H2}^{out}} \cdot Q_{in} \qquad \text{(Eqn. 8)}$$

where x_{H2}^{in} and x_{H2}^{out} are H_2 mixing ratios of the influent and effluent gases, respectively, and x_{CH4}^{out} is CH_4 mixing ratio of the effluent gas measured by the GC.

The total methane production rate (*MPR*; mol/hr) was calculated from GC measurements of x_{CH4}^{out} and Q_{out} calculated above:

$$MPR = \frac{P}{RT} \cdot Q_{\mathrm{out}} \cdot x_{CH4}^{out} \qquad \text{(Eqn. 9)}$$

where R is gas constant (8.314 $m^3 \cdot Pa/mol/K$), and T and P are temperature (K) and headspace pressure ($\approx 10^5$ Pa) during measurements. Cell-specific MPR (csMPR; mol/cell/hr) was calculated by dividing MPR by the total number of cells in the reactor:

$$\mathrm{cs}MPR = \frac{MPR}{N_{\mathrm{c}} \cdot V_{\mathrm{liq}}} \qquad \text{(Eqn. 10)}$$

where N_c is cell density (cells/m^3), V_{liq} is the volume of media (m^3).

2.3.7 Estimating dissolved H_2 concentrations in the liquid medium

For our experiments, the concentration of dissolved H_2, [H_2], is lower than what is expected from the saturation gas solubility and pH_2 in the influent gas. This is because of 1) high water vapor pressure in the reactor headspace during hyperthermophilic experiments and 2) the slow kinetics of H_2 dissolution from gas phase to liquid media. We considered the following to estimate [H_2].

Water vapor pressure in the reactor headspace, when saturated (pH_2O_{sat}), can be as high as 0.51 bars at 82 °C, 0.25 bars at 65 °C, and 0.20 bars at 60 °C (Haynes et al., 2016). If headspace gas was saturated with water vapor, pH_2 in the gas headspace for our fed-batch reactor can be lower by a factor of two compared to dry gas mixing ratios measured by GC. To consider the water vapor pressure in headspace (and bubbles), we estimated the pH_2O-corrected $pH_{2,VP}$ as:

$$p\mathrm{H}_{2,\mathrm{VP}} = x\mathrm{H}_2 \cdot (p_{reactor} - p\mathrm{H}_2\mathrm{O}_{\mathrm{sat}}) \qquad \text{(Eqn. 11)}$$

where $p_{reactor}$ is the total pressure of reactor, pH_2O_{sat} is the saturation water vapor pressure calculated as a function of temperature. The total pressure of reactor was assumed to be 1 bar. Headspace pressures were measured without inoculation and did not exceed over 1.05 bars.

In addition, the mass transport limit of H_2 from gas to dissolved phases can result in significant discrepancies between actual [H_2] and the [H_2] values expected at saturation with the gas phase H_2 (e.g., Pauss et al., 1990; Jud et al., 1997). The mass balance of H_2 for the liquid phase can be expressed as:

$$\frac{d[\mathrm{H_2}]}{dt} = -(\mathrm{H_2}\ \text{consumption rate}) + k_L a \cdot \left(K_\mathrm{H} p\mathrm{H}_{2,\mathrm{VP}} - [\mathrm{H_2}]\right) \qquad \text{(Eqn. 12)}$$

where H_2 consumption rate is 4 times the *MPR*, and k_La is the global mass transfer coefficient (e.g., hr^{-1}), which quantifies the rate of mass transfer for the whole reactor under a specific experimental condition. K_H is the Henry's law constant for H_2 (mol/L/Pa), calculated as a function of temperature and salinity following Chabab et al. (2020). The steady state solution for (Eqn. 12) is:

$$[\mathrm{H_2}] = \mathrm{K_H} \cdot pH_{2,\mathrm{VP}} - \frac{4 \cdot MPR}{k_L a} \qquad \text{(Eqn. 13)}$$

The values of k_La were estimated based on the following equation:

$$k_L a = \frac{D}{\delta \cdot V_\mathrm{liq}} \cdot a \qquad \text{(Eqn. 14)}$$

where D is the diffusivity coefficient for H_2 (m^2/hr); a is the sum of the surface area at the headspace-medium interface (A_h) and total surface area of bubbles (A_b) (m^2); and δ is the thickness of the diffusion layer (m). Using the δ values of 1 µm and 0.5 µm and other parameters specific to the experimental setup of this study (Table 2), k_La values of 380 and 760 hr^{-1} were used in (Eqn. 13) to calculate [H_2]. The parameter k_La is unique to a specific experimental condition and therefore varies between studies; however, the k_La range of 380 to 760 hr^{-1} falls reasonably within the ranges reported previously (e.g., 0.16 h^{-1}, Pauss et al., 1990; 220–1540 h^{-1}, Jud et al., 1997).

Following are brief justifications of the values used in Table 2. D is a typical diffusion coefficient for H_2 at 25 °C, 5.0×10^{-5} cm^2 sec^{-1} (Macpherson and Unwin, 1997). A_b is a function of the geometry and the number of bubbles, which is determined by the relationship between the size and residence time of bubbles and Q_{gas}. The upward velocity of bubbles for small bubbles (radius < 0.1 cm) was calculated following Park et al. (2017). The residence time and total volume of bubbles can be calculated for a known travel distance (i.e., height of the medium) and, from this, the total area of bubbles, A_b, was calculated. Finally, the surface area at the headspace-medium interface (A_h) is calculated from the reactor dimension.

2.3.8 Isotopologue flow network model

To examine the isotopologue data in this study with respect to the modeled [H_2] values, we applied the isotopologue flow network model adapted from Wang et al. (2015). The model calculates the expected isotopologue compositions of CH_4 as well as the intermediate carbon-containing species. During hydrogenotrophic methanogenesis (Eqn. 7), CO_2 is reduced to CH_4 via seven reactions and six intermediate carbon species. Following Wang et al. (2015) and Cao et al. (2019), we reduced the number of intermediate species to three by treating species with the same redox state as the same pool (Figure 2A). Two sets of input parameters required for the model are reversibilities (φ) for enzymatic reactions in the methanogenesis pathway and kinetic isotope effect (KIE) intrinsic to enzymatic reactions.

The first set of input parameters, metabolic reversibility (φ), is the ratio of backward to forward fluxes for an enzymatically-mediated reaction (Rees, 1973; Hayes, 2001). Previous models have used a range of φ values between 0 and 1, where $\varphi = 0$ is fully kinetic (non-equilibrium) and $\varphi = 1$ is fully reversible (equilibrium). Stolper et al., (2015) assumed $\varphi = 1$ for all except for the last H-addition step, which was varied. Wang et al. (2015) implemented a gradual and uniform departure from equilibrium (φ = 1→0) for all H-addition steps. Cao et al. (2019) tested binary cases, where φ is either 0 or 1 for each H-addition step. More recently, Gropp et al. (2021) re-evaluated these three models with calculated equilibrium fractionation factors and concluded that models in Wang et al. (2015) and Cao et al. (2019) can produce a range of carbon isotope fractionation observed in the natural environment with certain combinations of φ. This highlights the importance of φ, both in its degree of equilibrium at a given step and in its overall variation among the four H-addition steps, in determining the outputs of isotopologue flow network models. In this work, we parameterized φ values for the four H-addition steps as a function of H_2 by assuming Michaelis–Menten kinetics, as described in Wang et al. (2015):

$$\varphi_n = 1 - \frac{[H_2]}{K_{m,n} + [H_2]} \qquad \text{(Eqn. 15)}$$

where n=1 to 4, representing the four H-addition steps (Figure 2A), and $K_{m,n}$ is the effective half-saturation constant. According to the model for the energy conservation of hydrogenotrophic methanogenesis, the last step (reduction of methyl-CoM to CH_4) is exergonic and expected to be less reversible compared to other steps (Thauer et al., 2008; Thauer, 2011; Ono et al., 2022).

We modeled differential reversibility by changing the $K_{m,n}$ values (Eqn. 15) and compared the following three cases:

1) equilibrium end-member scenario with a high $K_{m,n}$ of 10^4 M for all reactions (n=1 to 4),
2) uniform reversibility scenario with a $K_{m,n}$ of 5×10^{-5} M for all reactions (n=1 to 4), and
3) differential reversibility scenario with a $K_{m,n}$ of 5×10^{-5} M for the first three reactions (n=1 to 3) and a $K_{m,4}$ of 10^{-8} M (less reversible) for the last reaction.

The K_m value of 5×10^{-5} M approximates the experimentally determined K_m values for hyperthermophilic methanogens (66 μM for three *Methanocaldococcus* species; Ver Eecke *et al.*, 2012). The lower K_m value of 10^{-8} M makes the last reversible step largely unidirectional down to a low [H_2] of ~10^{-8} M. For reference, the minimum threshold pH_2 estimated for pure cultures is 6.5 Pa (*ca*. 5×10^{-8} M at 25 °C), and the theoretical pH_2 at thermodynamic equilibrium for hydrogenotrophic methanogenesis is 0.1 Pa (*ca*. 1×10^{-9} M at 25 °C) assuming [CO_2]/[CH_4] = 1 (Lovley, 1985; Thauer et al., 2008).

The values of KIEs are the second set of required input parameters for the model. KIEs are experimentally determined only for the last reaction catalyzed by methyl-coenzyme M reductase (Scheller et al., 2013). KIEs for other reactions are chosen to reproduce the kinetic end-member solution and maintain the consistency with equilibrium fractionations (Supplementary Material; Table S1). Equilibrium fractionation factors (α^{eq}) estimated by quantum mechanical calculation (Gropp et al., 2021; Ono et al., 2021) constrain the model solution for the equilibrium end-member scenario (Figure 2B). We use α^{eq} values estimated at 82 °C (experimental temperature for B.82 and F.82.80) by Gropp et al. (2021) for fractionations between intermediates and $H_2O_{(g)}$ or $CO_{2,(g)}$. Then, α^{eq} values against $H_2O_{(l)}$ were calculated from those against $H_2O_{(g)}$, using experimentally derived α values between $H_2O_{(l)}$ and $H_2O_{(g)}$ (Horita and Wesolowski, 1994).

3 Results

3.1 Batch culture experiment

The trends observed with increasing $\delta^{13}C_{CH4}$ values and decreasing δD_{CH4} and $\Delta^{13}CH_3D$ values (Table 3) were consistent with those previously reported for a batch culture experiment with *M. bathoardescens* (Gruen et al., 2018). The carbon, hydrogen and clumped isotope fractionation factors ($^{13}\alpha$, $^{2}\alpha$ and γ, respectively) calculated following Gruen et al. (2018) were comparable to those reported previously (Supplementary Material, Figure S1D, S1E and S1F).

3.2 Fed-batch culture experiments (*M. bathoardescens*)

The growth of *M. bathoardescens* in fed-batch experiments were characterized by linear increase in cell density (Supplementary Material, Figure S2A, S2D and S2G), consistent with previous observations with *M. bathoardescens* in fed-batch experiments (Ver Eecke et al., 2012). $^{13}\alpha$ decreased from 0.957 to 0.944 during F.82.80 (82 °C, 80% H_2; Figure 3A4; Figure 4A) and from 0.982 to 0.964 during F.60.80 (60 °C, 80% H_2; Figure 3B4; Figure 4A). $^{2}\alpha$ increased from 0.674 to 0.708 during F.82.80 (Figure 3A5; Figure 4B) and from 0.672 to 0.730 during F.60.80 (Figure 3B5; Figure 4B). $\Delta^{13}CH_3D$ values decreased from 1.25 ± 0.48‰ to –0.29 ± 0.47‰ during F.82.80 (Figure 3A6; Figure 4C) and from 1.52 ± 0.58‰ to 0.06 ± 0.17‰ during F.60.80 (Figure 3B6; Figure 4C). These $\Delta^{13}CH_3D$ values are lower than those expected at equilibrium (4.1‰ at 82 °C and 4.6‰ at 60 °C). Notably, the changes in $\Delta^{13}CH_3D$ were in the direction away from the values expected at equilibrium, unlike $^{13}\alpha$ and $^{2}\alpha$ values that changed toward equilibrium values. The changes in bulk isotope values ($\delta^{13}C_{CO2}$, $\delta^{13}C_{CH4}$, δD_{H2O} and δD_{CH4}) during F.82.80, F.60.80 and F.82.25 are reported in Table 4 and Supplementary Material, Figure S3. Note that, for F.82.25, the absolute $\delta^{13}C_{CH4}$ values for F.82.25 are higher compared to those of F.82.80 because different sources of CO_2 were used for the experiments.

3.3 Fed-batch culture experiments (*M. thermautotrophicus*)

The growth patterns of *M. thermautotrophicus* in fed-batch experiments were characterized by distinct periods of exponential growth during the first 26 and 12 hours for F.65.20 (65 °C, 20% H_2) and F.65.5 (65 °C, 5% H_2), respectively (Supplementary Material, Figure S4A and S4D). For F.65.5, xH₂ in the supply gas was decreased from 5% to 1.6% after 55 hours, such that enough biomass can be established at 5% H_2 before further decreasing the xH_2 to 1.6% (minimum xH_2

achievable with the experimental setup). After decreasing the xH_2 to 1.6%, the cell density remained relatively constant for the remainder of the experiment, and xCH_4 and cs*MPR* decreased (Supplementary Material, Figure S4F; Table 5). $^{13}\alpha$ decreased from 0.966 to 0.950 during F.65.20 and from 0.957 to 0.938 during F.65.5 (Figure 3D4 and 3E4; Figure 4A). $^{2}\alpha$ slightly increased during F.65.20 and did not change significantly during F.65.5 (Figure 3D5 and 3E5; Figure 4B). $\Delta^{13}CH_3D$ values decreased over time, moving away from that expected at equilibrium, as was observed in *M. bathoardescens* experiments (Figure 3D6 and 3E6; Figure 4B). Notably, the magnitudes of depletion (i.e., low $\Delta^{13}CH_3D$ values) observed during F.65.20 and F.65.5 are comparable to those observed during batch experiments with mesophilic methanogens, which tend to produce lower $\Delta^{13}CH_3D$ values compared to thermophilic methanogens (open *vs*. filled circles; Figure 4C). The changes in bulk isotope values ($\delta^{13}C_{CO2}$, $\delta^{13}C_{DIC}$, $\delta^{13}C_{CH4}$, δD_{H2O} and δD_{CH4}) during F.65.20 and F.65.5 are reported in Table 5 and Supplementary Material, Figure S5.

3.4 Dissolved H_2 in the liquid medium

The results of $[H_2]$ calculations are shown in Figure 3. Overall, the results show undersaturation in $[H_2]$ with respect to headspace for high density and fast-growing cultures (Figure 3A1–4E1). Media become more undersaturated over time (i.e., at higher cell density; Figure 3A2–3E2) due to the increase in total H_2 consumption rate, which corresponds with the increase in *MPR* (Figure 3A3–3E3). The difference between the maximum $[H_2]^{eq}$ and minimum $[H_2]$ values (with lower k_La) was the largest, between 2-fold and >10-fold, at the highest temperature (82 °C; F.82.80 and F.82.25), whereas the difference was <2-fold at lower temperatures of 65°C and 60°C. The lower range of $[H_2]$ was calculated using the minimum k_La value required to avoid a negative $[H_2]$ in all experiments (350 h^{-1}), and the higher range of $[H_2]$ was calculated with a k_La value of 350 h^{-1}, twice as much as the minimum value (Figure 3A3–3E3).

3.5 Isotopologue flow network model

The equilibrium end-member scenario shows uniform values across the [H_2] range that correspond to values expected at equilibrium (–51‰ for $\delta^{13}C$, –151‰ for δD and 6‰ for $\Delta^{13}CH_3D$ at 82 °C, yellow dotted lines; Figure 5). The isotope values change as a function of [H_2] in the uniform reversibility and differential reversibility scenarios (red dashed line and blue solid line, respectively; Figure 5). The $\delta^{13}C$ and $\Delta^{13}CH_3D$ profiles show significant difference between uniform and differential reversibility scenarios; in the differential reversibility scenario, $\delta^{13}C$ and $\Delta^{13}CH_3D$ values decrease to local minima with decreasing [H_2] at a [H_2] range between the two K_m values assigned (i.e., $K_{m,1–3} = 5\times10^{-5}$ M and $K_{m,4} = 10^{-8}$ M; Figure 2D), and values increase toward the equilibrium values with decreasing [H_2] when all four steps become reversible ([H_2] $\lesssim 10^{-7}$ M) (Figure 5A and 5C). The low $\delta^{13}C$ values between the two K_m values are less than the value expected for equilibrium. On the other hand, the model predicts that δD values increase monotonically toward equilibrium with decreasing [H_2], and uniform and differential reversibility scenarios were similar overall. In the differential reversibility scenario, δD show two inflection points corresponding to the two different K_m values ($K_{m,1–3}$ 5×10^{-5} M and $K_{m,4}$ of 10^{-8} M). In the Discussion section below, we provide further interpretations for the patterns of isotope fractionation factors ($^{13}\alpha$, $^{2}\alpha$) and clumped isotopologue abundance ($\Delta^{13}CH_3D$) observed during fed-batch experiments in this study in light of [H_2] and isotopologue flow network model results.

4 Discussion

Our results—from combined analyses of $\delta^{13}C_{CO2}$, $\delta^{13}C_{CH4}$, δD_{H2O}, δD_{CH4} and $\Delta^{13}CH_3D$—confirm previous observations that $^{13}\alpha$ values decrease with decreasing pH_2 (Penning et al., 2005; Londry et al., 2008; Okumura et al., 2016; Topçuoğlu et al., 2019; Nguyen et al., 2020) and shed some new light on the behavior of hydrogen isotope and clumped isotopologue systems at different growth phases and [H_2]. The observed values of consistently low δD_{CH4} and $\Delta^{13}CH_3D$ (relative to equilibrium) suggest primarily kinetic fractionations for hydrogen and clumped isotope systems under our experimental conditions. However, the apparent decrease in $\Delta^{13}CH_3D$ values (i.e., further departure from equilibrium) for later growth phase and low [H_2] was unexpected and contrasts previous model predictions based on the differential reversibility hypothesis (e.g., Stolper et al., 2015; Wang et al., 2015). Using the modeled values of [H_2] in the fed-batch system and results of isotopologue flow network model, we discuss the observed patterns of $^{13}\alpha$ (section 4.1); $^{2}\alpha$ and $\Delta^{13}CH_3D$ (section 4.2); limitations of the model and broader implications for interpreting the isotopic signatures of natural methane samples (section 4.3).

4.1 High cell density during stationary growth phase leads to low [H_2] and lower than equilibrium $^{13}\alpha$

Lower $^{13}\alpha$ values (larger carbon isotope fractionation) were observed during later growth phase within a single experiment and at lower xH_2 across experiments (Figure 3A4–3E4; Figure 4A). The decrease in $^{13}\alpha$ coincides with the transition from exponential phase to stationary phase for *M. thermautotrophicus* (Figure 3D2 and 3E2) or later linear growth for *M. bathoardescens* (Figure 3A2–3C2). Our observation is consistent with previous culture studies that reported decreasing $^{13}\alpha$ values as a function of growth phase (e.g., Botz et al., 1996; Valentine et al., 2004) and experiments with lower pH_2 (Valentine et al., 2004; Londry et al., 2008; Okumura et al., 2016; Topçuoğlu et al., 2019; Nguyen et al., 2020). Some studies have also reported $^{13}\alpha$ values lower than equilibrium value (i.e., larger than equilibrium isotope fractionation) (e.g., Botz et al., 1996; Valentine et al., 2004; Penning et al., 2005; Okumura et al., 2016; Topçuoğlu et al., 2019), similar to the observations in this study (e.g., F.82.80, F.82.25 and F.65.5 in Figure 3A4–3E4 and Figure 4A).

In addition to causing physiological changes, later growth phase with high cell density leads to low [H_2] due to the increase in total H_2 consumption rate. The decrease in [H_2] at high cell density is important to consider for the hydrogenotrophic methanogenesis reaction because of its 4:1 H_2:CH_4 stoichiometry (Eqn. 7) and poor solubility of H_2. While the dissolved concentrations of highly soluble gases (e.g., CO_2) can be close to equilibrium with the headspace, the dissolved concentrations of poorly soluble gases (e.g., H_2 and CH_4) can be far away from equilibrium with the gas phase. Higher partial pressure of water vapor at saturation (pH_2O_{sat}) in the reactor headspace during (hyper)thermophilic incubations should also be considered (Eqn. 11), as it would further lower the [H_2] in liquid media. The observed linear growth for *M. bathoardescens* (Figure 3A2–3C2) suggests that growth and methane production rates were limited by the supply (=dissolution) rate of H_2.

Accurate measurement of [H_2] for methanogenic media can be challenging. Previous studies measured [H_2] for fed-batch reactors or chemostats by sampling liquid media into serum vials and measuring pH_2 in the headspace (e.g., Ver Eecke et al., 2012; Stewart et al., 2016; Topçuoğlu et al., 2018, 2019). For example, Topçuoğlu et al. (2019) reported [H_2] values (prior to inoculation) of 82 ± 2 and 21 ± 6 µM for high and low H_2 experiments, respectively. These values are lower and higher than the saturation concentrations (516 and 10 µM) based on the dry H_2 mixing ratios of 86.6 and 1.6% for high and low H_2 experiments, respectively. Here, high pH_2O_{sat} at higher temperatures (0.51 bars at 82°C) can explain lower [H_2] compared to calculations for dry headspace. Higher than saturation [H_2] values may indicate entrainment of H_2 microbubbles in addition to dissolved H_2 (e.g., McGinnis et al., 2015). After inoculation, microbial consumption of H_2 would affect the steady state dissolved concentrations of gases in the liquid due to relatively slow rate of H_2 dissolution (Eqn. 12). For example, in anaerobic fermentors where H_2 is produced by microbial processes, the liquid-to-gas mass transport limit resulted in as much as 80 times oversaturation of H_2 compared to the headspace gas (Pauss et al., 1990). On the other hand, in chemostat cultures where methanogens consume H_2 (i.e., gas-to-liquid transport), the dissolved H_2 concentration was found to be 10 times lower than the saturation with respect to gas phase (Jud et al., 1997). Because methanogens use dissolved form of H_2, we estimated [H_2] under each experimental condition to assess the effect of the dissolved H_2 concentration on isotope fractionation.

As shown in Figure 6A, the modeled [H_2] range under our experimental conditions (*ca*. 7 to 410 µM) is lower than the [H_2] range expected for typical batch cultures (e.g., 0.6 to 1.2 mM for 1 to 2 bars of 80% H_2 headspace) and partially overlaps with the [H_2] range found in cow rumen (0.1 to 50 µM; Smolenski and Robinson, 1988; Janssen, 2010, and references therein; Wang et al., 2015); but it is higher than the [H_2] range found in typical freshwater (5 to 75 nM; Robinson and Tiedje, 1982; Conrad et al., 1985; Conrad et al., 1987; Kuivila et al., 1989) and marine sediments (2 to 60 nM; Novelli et al., 1987; Lin et al., 2012). In the differential reversibility scenario for the isotopologue flow network model, $\delta^{13}C$ values decrease with a decrease in [H_2] for [H_2] <1 mM (between 10^{-6} and 10^{-3} M; Figure 5A). This is consistent with the decreasing $^{13}\alpha$ values observed during fed-batch experiments with a decrease in [H_2] (due to increase in cell density) or $x\mathrm{H_2}$ (mixing ratios for different experiments) for the modeled [H_2] range between 7 and 410 µM (between 7×10^{-6} and 4×10^{-4} M; Figure 6B). In addition, the $^{13}\alpha$ values during the fed-batch experiment conducted at 82 °C and 80% H_2 (F.82.80; $^{13}\alpha = 0.95 \pm 0.01$; Table 4, Figure 4A) were lower compared to the $^{13}\alpha$ value for batch experiment conducted at the same temperature and initial $x\mathrm{H_2}$ (B.82.80; $^{13}\alpha = 0.98$; Supplementary Material, Figure S1D). Considering that [H_2] in batch cultures at high headspace pressure (1 to 2 bars) and $x\mathrm{H_2}$ (80%) can reach millimolar levels (0.6

to 1.2 mM; Figure 6A), the difference in $^{13}\alpha$ values observed between fed-batch and batch experiments is also consistent with the overall correlation between low $^{13}\alpha$ and low [H_2]. Similarly, the difference in $^{13}\alpha$ observed between F.60.80 and F.82.80, despite the same $x$$H_2$ of 80%, may be explained by the difference in [H_2]. Because of lower temperature and pH_2O_{sat}, [H_2] is significantly higher at 60 °C compared to that at 82 °C (e.g., Figure 3A1 *vs*. 3B1).

Besides the general correlation between low [H_2] and low $^{13}\alpha$ values, our isotopologue flow network model reproduced $^{13}\alpha$ values lower than equilibrium value (i.e., larger than equilibrium fractionation) observed during later growth phases in the differential reversibility scenario (Figure 5A). When [H_2] is between 5×10^{-5} and 10^{-8} M (i.e., $K_{m,1–3}$ and $K_{m,4}$, respectively), reactions up to CH_3-CoM are largely reversible (φ_1 to $\varphi_3 \simeq 1$). As a result, $\delta^{13}C$ of the methyl group of CH_3-CoM approaches to equilibrium value (–52‰ at 82°C; Gropp et al., 2021). The reversibility of the last step is relatively low above 10^{-8} M H_2 in our model, and this step can result in kinetic isotope fractionation of up to –40‰ ($^{13}\alpha = 0.96 \pm 0.01$, assayed at 60 °C; Scheller et al., 2013). Accordingly, the maximum overall fractionation of ~–92‰ (= –52 – 40‰) can be achieved when the first three steps are fully reversible (φ_1 to $\varphi_3 \simeq 1$) and the last step is fully kinetic ($\varphi_4 \simeq 0$). This is consistent with the minimum $^{13}\alpha$ value (0.908, or fractionation of –92‰) in the differential reversibility scenario simulated at 60 °C in our study (yellow solid line; Figure 6B). Previous studies have also reported lower than equilibrium $^{13}\alpha$ values, which were interpreted as the growth phase effect (e.g., Botz et al., 1996). The non-monotonic nature of carbon isotope fractionation as a function of [H_2] has been recently suggested in model studies (Gropp et al., 2021; Gropp et al., 2022; Ono et al., 2022). This study provides an experimental demonstration of the production of $^{13}\alpha$ values lower than the equilibrium value. At much lower [H_2] (i.e., $<10^{-8}$ M), the last step of methanogenesis becomes reversible and equilibrium fractionation is expected (–57‰ at 60 °C, –51‰ at 82 °C;

Figure 6B). Future experiments under a sub-μM [H_2] range are needed to validate the increase in $^{13}\alpha$ values toward the equilibrium value that is predicted by the model.

4.2 Differential reversibility can explain the observed hydrogen and clumped isotopologue systematics

Previous culture studies have so far exclusively produced non-equilibrium hydrogen isotope fractionation (Valentine et al., 2004; Yoshioka et al., 2008; Hattori et al., 2012; Kawagucci et al., 2014; Stolper et al., 2015; Okumura et al., 2016; Gruen et al., 2018). In this study, $^{2}\alpha$ values significantly lower than equilibrium value were observed ($^{2}\alpha$ = 0.69 ± 0.02, Figure 3A5–3E5, Figure 4B *vs*. $^{2}\alpha^{eq}$ = 0.81 at 60 °C and 0.82 at 82 °C). In the differential reversibility scenario (blue solid line; Figure 5B), δD values stay relatively constant for the [H_2] range between 5×10^{-5} and 10^{-8} M (i.e., $K_{m,1-3}$ and $K_{m,4}$, respectively) and significantly increase toward equilibrium value with decreasing [H_2] for [H_2] ≤ 10^{-8} M. This is consistent with our isotope data for fed-batch experiments for the modeled [H_2] range between 7 and 410 μM (between 7×10^{-6} and 4×10^{-4} M), where relatively constant $^{2}\alpha$ values were observed (Figure 6C).

The relatively constant $^{2}\alpha$ for modeled [H_2] between 10^{-5} M and 10^{-8} M in the differential reversibility scenario (Figure 5B) and observed in our experiments (Figure 6C) can be explained with a large KIE associated with the last step of methanogenesis (CH_3-CoM to CH_4 reduction; reaction 4, Figure 2A). As described above in section 4.1, reactions up to CH_3-CoM are reversible (φ_1 to $\varphi_3 \simeq 1$) in the differential reversibility scenario for the [H_2] range between 5×10^{-5} and 10^{-8} M. Consequently, the three H atoms in the methyl group of CH_3-CoM are isotopically equilibrated with the surrounding water ($\delta D_{CH3-CoM}$ = –122‰ at 82 °C; Gropp et al., 2021). The reversibility of the last step is relatively low at [H_2] ≥ 10^{-8} M in our model, and this step can result in large kinetic isotope fractionation. For reference, Scheller et al., (2013) reported experimentally determined values of primary KIE (k_H/k_D) of 2.44 (i.e., $^{2,P}\alpha$ of 0.41) and secondary KIE of 1.17 (i.e., $^{2,S}\alpha$ of 0.85) at 60 °C for the last step in reverse direction. The addition of the last H atom from water (e.g., δD_{H2O} = –50‰) to the equilibrated CH_3-CoM with the $^{2,P}\alpha$ and $^{2,S}\alpha$ values above would result in the final δD_{CH4} of –343‰ (= [¾ · (–122/1000+1) · (0.85) + ¼ · (–50/1000+1) · (0.41)] – 1), which is comparable to the range observed in our experiments (–339 ± 34‰; Table 4; Table 5).

These experimental and model results together suggest that the persistent non-equilibrium signatures observed for hydrogen isotope system in this study and previous studies are results of differential reversibility with a lower reversibility (larger KIE) at the last H-addition step. It follows that, in our model setup, hydrogen isotope fractionation approaches to equilibrium values at sub-μM ranges of [H_2] (solid line, Figure 6C). Future experiments with direct measurements and precise control of [H_2] (e.g., continuous cultures) at sub-μM levels are needed to validate this hypothesis.

The distinct pattern of decreasing $\Delta^{13}CH_3D$ values observed for clumped isotope system (Figure 3A6–3E6; Figure 6D) is in sharp contrast with previous isotope model results. Previous studies suggest a positive correlation among the overall metabolic reversibility, $^2\alpha$ and $\Delta^{13}CH_3D$, and this relationship has been used to explain experimental and environmental data (e.g., Stolper et al., 2015; Wang et al., 2015; Douglas et al., 2017). In this study, $\Delta^{13}CH_3D$ values decreased with decreasing [H_2] (higher reversibility), and this pattern was reproduced in the differential reversibility model scenario (blue solid line, Figure 5C). The major difference from previous model results is attributed to the decreasing pattern of $\Delta^{13}CH_3D$ observed for the [H_2] range of 10^{-6} to 10^{-3} M (Figure 6D), which is lower than the range expected for typical batch cultures and partially overlaps with the range found in cow rumen (Figure 6A). Previous culture studies are limited to end-point batch experiments, e.g., 0.6 to 1.2 mM for 1 to 2 bars of 80% H_2 headspace (Stolper et al., 2015; Wang et al., 2015; Young et al., 2017; Gruen et al., 2018; Giunta et al., 2019). Thus, more culture studies in fed-batch systems or continuous cultures at [H_2] spanning from $\leq 10^{-6}$ to 10^{-3} M would help resolve the discrepancy between different model predictions about the relationship between $^2\alpha$ and $\Delta^{13}CH_3D$.

It is worth noting that the two inflection points in the $\Delta^{13}CH_3D$ profile occur around $K_{m,1-3}$ of 5×10^{-5} and $K_{m,4}$ of 10^{-8} M. The effect of assigned K_m values on the $\Delta^{13}CH_3D$ profile was evident from sensitivity test results (Supplemental Material, Figure S6). $K_{m,1-3}$ of 5×10^{-5} M resulted in the best fit to the $\Delta^{13}CH_3D$ values measured from the fed-batch experiments in this study (e.g., panel C *vs*. panels A, B, D or E; Supplemental Material, Figure S6). This is likely not a coincidence, given that the experimentally determined K_m value for hyperthermophilic methanogens is close to the assigned value (6.6×10^{-5} M for three *Methanocaldococcus* species; Ver Eecke *et al.*, 2012). Because our experiments were done at the modeled [H_2] range between 7 and 410 μM, we cannot empirically assess the fit of the lower $K_{m,4}$ value in the differential reversibility scenario. For example, varying $K_{m,4}$ between 10^{-10} and 10^{-6} M has negligible effect on the $\Delta^{13}CH_3D$ profile for [H_2] $\geq 10^{-6}$ M; for [H_2] $\leq 10^{-6}$ M, however, the $\Delta^{13}CH_3D$ profile changes such that the [H_2] at which $\Delta^{13}CH_3D$ reaches equilibrium depends on $K_{m,4}$ (panels F–J; Supplemental Material, Figure S6). Future experiments at sub-μM levels of [H_2] are needed to properly determine the threshold $K_{m,4}$ value for the last step of methanogenesis (which may depend on the species) that would equilibrate $\Delta^{13}CH_3D$ signatures from hydrogenotrophic methanogenesis. However, the $K_{m,4}$ value of 10^{-8} M used in this study is reasonable, considering that equilibrium $\Delta^{13}CH_3D$ signatures in microbial methane have been found in marine sediments where the typical [H_2] range is between 2 and 60 nM (Novelli et al., 1987; Lin et al., 2012; Figure 6A).

Another characteristic pattern of the clumped isotope system observed in our experiments was significant depletion in $^{13}CH_3D$ with anti-clumped (negative) $\Delta^{13}CH_3D$ values at low $[H_2]$ or xH_2 (Figure 3A6–3E6; Figure 6D). The differential reversibility scenarios shown in Figure 5C and Figure 6D successfully reproduce not only the decreasing trend but also anti-clumped $\Delta^{13}CH_3D$ values that fit the range of $\Delta^{13}CH_3D$ values observed in this study (minimum of –4.1‰). Sensitivity test results indicated that secondary clumped isotope fractionation of ≥6‰ (i.e., ${}^{S}\gamma \geq 0.994$) is required to produce a distinct decreasing pattern with negative $\Delta^{13}CH_3D$ values at $[H_2] \geq 10^{-5}$ M (i.e., lower end of our experimental range) (panels A–F; Supplemental Material, Figure S7). The ${}^{S}\gamma$ value of 0.990 (i.e., 10‰ secondary clumped isotope fractionation) resulted in the profile that best fits both the decreasing trend and magnitude of depletion in measured $\Delta^{13}CH_3D$ values (Figure 5C, Figure 6D). Varying the magnitude of primary clumped isotope fractionation (${}^{P}\gamma$) without any secondary isotope fractionation (${}^{S}\gamma=1$) did not reproduce the observed patterns in $\Delta^{13}CH_3D$ (panels G–L; Supplemental Material, Figure S8).

4.3 Limitations of the isotopologue flow network model and implications for interpreting the isotope signatures of natural methane samples

Overall, our results are in general agreement with previous studies regarding the importance of $[H_2]$ and the growth phase as controlling factors of bulk isotope signatures (e.g., Games and Hayes, 1978; Fuchs et al., 1979a; Belyaev et al., 1983; Balabane et al., 1987; Krzycki et al., 1987; Botz et al., 1996; Valentine et al., 2004; Penning et al., 2005; Londry et al., 2008; Yoshioka et al., 2008; Hattori et al., 2012; Okumura et al., 2016; Topçuoğlu et al., 2019; Nguyen et al., 2020) as well as clumped isotope signatures (e.g., Stolper et al., 2015; Wang et al., 2015; Douglas et al., 2020).

While we explored three different cases—including the differential reversibility scenario—for the isotopologue flow network model, there is much complexity associated with the biochemical inner workings of methanogenesis that is not captured in the model. The model uses a constant KIE value per H-addition step, assuming that each step is catalyzed by the same enzyme across the range of [H_2] examined in this study (10^{-9} to 10^{-2} M). This may not be true for H-addition steps that can be catalyzed by more than one enzyme (i.e., isoenzymes). There are at least two sets of isoenzymes known to catalyze the second and fourth H-addition steps during hydrogenotrophic methanogenesis. The fourth step of methanogenesis (the reduction of methenyl-H_4MPT^+ to methylene-H_4MPT) involves either the oxidation of H_2 or the oxidation of the reduced form of F_{420} ($F_{420}H_2$), where the former is catalyzed by H_2-forming N^5,N^{10}-methylene-H_4MPT dehydrogenase (Hmd) and the latter is catalyzed by F_{420}-dependent N^5,N^{10}-methylene-H_4MPT dehydrogenase (Fmd) (von Bünau et al., 1991; Reeve et al., 1997). Previous studies have shown that Mtd increases in expression, relative to Hmd, under H_2 limitation (Reeve et al., 1997; Hendrickson et al., 2007; Topçuoğlu et al., 2019). The isoenzyme switching from Hmd to Mtd under H_2 limitation has been suggested to allow a greater expression of carbon isotope fractionation (Valentine et al., 2004) and may apply for hydrogen and clumped isotope systems as well.

Another set of isoenzymes, MCR I and MCR II (sometimes referred to as MR I and MR II), catalyzes the fourth and last H-addition steps of hydrogenotrophic methanogenesis (Pihl et al., 1994; Reeve et al., 1997). The relative abundances of MCR I and MCR II have been shown to be determined largely by growth phase, where MCR II is preferentially expressed during exponential phase and MCR I during linear or stationary phase (Rospert et al., 1990; Bonacker et al., 1992; Pihl et al., 1994). Whether distinct KIEs are associated with these isoenzymes remains unclear; however, considering that MCR I and MCR II have different substrate affinities (i.e., K_m values for CH_3-S-CoM and H-S-HTP) and catalytic rates (Bonacker et al., 1993), it is possible that these isoenzymes for the rate-limiting step of last H-addition impart distinct KIEs. Future studies combining a proteomic or transcriptomic approach and isotope analyses are needed to evaluate the effect of isoenzyme switching on isotope fractionation during hydrogenotrophic methanogenesis.

Despite the limitations mentioned above, insights gained from the empirical relationships among bulk ($^{13}\alpha$, $^{2}\alpha$) and clumped ($\Delta^{13}CH_3D$) isotope systems investigated in this study help us better understand isotope fractionation during hydrogenotrophic methanogenesis and to interpret the isotope signatures of natural methane samples. Several studies suggested AOM as the mechanism for equilibration of $\Delta^{13}CH_3D$ and $\Delta^{12}CH_2D_2$ values of microbial methane (Ash et al., 2019; Giunta et al., 2019; Zhang et al., 2021). A recent controlled culture study has shown that KIE associated with AOM can drive the $\Delta^{13}CH_3D$ value of residual methane toward and even beyond values expected for internal equilibrium (Ono et al., 2021). Results of this study further elucidate whether (near-)equilibrium isotope signatures in microbial methane require re-equilibration by external processes such as anaerobic oxidation of methane (AOM). The model results in this study indicate that a very low (sub-nM) [H_2] may be required to achieve near-equilibrium $\Delta^{13}CH_3D$ under our experimental conditions (Figure 5C), and methanogenesis may not occur at this low [H_2] (e.g., Hoehler et al., 2001; Ono et al., 2022). While this conclusion does not exclude the possibility of methanogenesis-driven equilibration of $\Delta^{13}CH_3D$, it highlights the challenge of relating certain isotopologue signals to specific metabolisms.

The non-monotonic trajectory of $\Delta^{13}CH_3D$ predicted for hydrogenotrophic methanogenesis may have important implications for interpreting natural methane samples from a broader range of environments. In general, natural samples from freshwater ecosystems show clumped isotope abundances that indicate strong KIE (Stolper et al., 2015; Wang et al., 2015; Douglas et al., 2016; Young et al., 2017; Gruen et al., 2018; Giunta et al., 2019; Douglas et al., 2020). The lowest value of clumped isotope abundance measured from laboratory cultures so far is a $\Delta^{13}CH_3D$ value of –6.4‰ from a *Methanosarcina acetivorans* culture grown on methanol (Douglas et al., 2020). In freshwater environments, methanogenesis pathways besides the hydrogenotrophic pathway (i.e., acetoclastic and methylotrophic pathways) are considered more widespread compared to marine environments. Currently, a leading hypothesis regarding the interpretation of freshwater microbial methane clumped isotope signatures is that Δ_{18} and $\Delta^{13}CH_3D$ signatures are primarily controlled by methane production rates, irrespective of the biochemical pathway. For example, Douglas et al. (2020) presented isotope model trajectories where Δ_{18} and $\Delta^{13}CH_3D$ values of pure and enrichment cultures of methanogens using different substrates (H_2/CO_2, trimethylamine, acetate, and methanol) monotonically increases with decreasing methane production rates. If the non-monotonic trajectory of $\Delta^{13}CH_3D$ during hydrogenotrophic methanogenesis predicted in this study applies similarly to other methanogenic pathways as a function of substrate concentration, existing interpretative frameworks may need to be updated accordingly.

5 Conclusion

We cultured two different species of methanogens, *Methanocaldococcus bathoardescens* and *Methanothermobacter thermautotrophicus* (ΔH), in batch and fed-batch systems and measured the $\delta^{13}C$ and δD of the substrates (CO_2 and H_2O) as well as the $\delta^{13}C$, δD and $\Delta^{13}CH_3D$ of the product (CH_4). The results of the fed-batch experiments confirm previous observations, where carbon isotope fractionation ($^{13}\alpha = 0.96 \pm 0.02$) approaches and often exceed the magnitude expected at CH_4-CO_2 equilibrium (e.g., Botz et al., 1996; Valentine et al., 2004; Penning et al., 2005; Okumura et al., 2016; Topçuoğlu et al., 2019), while hydrogen isotope fractionation remains significantly larger ($^{2}\alpha = 0.67 \pm 0.01$) than that expected at CH_4-H_2O equilibrium (Figure 4). The observed low $\Delta^{13}CH_3D$ values indicate kinetic isotope effects, with an apparent decrease in $\Delta^{13}CH_3D$ values with decreasing pH_2. The isotopologue flow network model presented showed our observations—large carbon isotope fractionation, depleted hydrogen isotope signatures, and distinct decreasing $\Delta^{13}CH_3D$ values with decreasing pH_2—can be explained by differential reversibility, in which the last step of methanogenesis is less reversible compared to the preceding three H-addition reactions. In addition, including secondary clumped KIE in the model reproduced the magnitude of depletion in $\Delta^{13}CH_3D$ values observed in our experiments. Future studies focusing on controlled H_2 limitation experiments at sub-μM concentrations and conducting proteomic or transcriptomic analyses in parallel may improve our interpretations of the bulk and clumped isotope signatures used for methane source identification.

Acknowledgment

We thank J. F. Holden (University of Massachusetts, Amherst) for providing the *M. bathoardescens* culture used in this study; T. Bosak for providing lab facilities to support our culturing work; J. Sun for laboratory assistance for *M. thermautotrophicus* experiments; and D. Boutt (University of Massachusetts, Amherst) for analyzing δD_{H2O}. This work was supported by the NASA Astrobiology Institute "Rock-Powered Life" project under cooperative agreement NNA15BB02A. J.H.R. was also supported by the Grayce B. Kerr Fellowship, the Robert R. Shrock Fellowship and the Callahan Dee Fellowship at MIT.

Appendix A. Supplementary Material

Research Data that supports this research publication can be found in the Supplementary Material at [Link].

References

Ash J. L., Egger M., Treude T., Kohl I., Cragg B., Parkes R. J., Slomp C. P., Lollar B. S. and Young E. D. (2019) Exchange catalysis during anaerobic methanotrophy revealed by 12CH2D2 and 13CH3D in methane. *Geochemical Perspect. Lett.* **10**, 26–30.

Balabane M., Galimov E., Hermann M. and Létolle R. (1987) Hydrogen and carbon isotope fractionation during experimental production of bacterial methane. *Org. Geochem.* **11**, 115–119.

Baldassare F. J., McCaffrey M. A. and Harper J. A. (2014) A geochemical context for stray gas investigations in the northern Appalachian Basin: Implications of analyses of natural gases from Neogene-through Devonian-age strata. *Am. Assoc. Pet. Geol. Bull.* **98**, 341–372.

Belyaev S. S., Wolkin R., Kenealy W. R., DeNiro M. J., Epstein S. and Zeikus J. G. (1983) Methanogenic Bacteria from the Bondyuzhskoe Oil Field: General Characterization and Analysis of Stable-Carbon Isotopic Fractionation. *Appl. Environ. Microbiol.* **45**, 691–697.

Bigeleisen J. (1955) Statistical mechanics of isotopic systems with small quantum corrections. I. general considerations and the rule of the geometric mean. *J. Chem. Phys.* **23**, 2264–2267.

Bonacker L. G., Baudner S., Mörschel E., Böcher R. and Thauer R. K. (1993) Properties of the two isoenzymes of methyl-coenzyme M reductase in Methanobacterium thermoautotrophicum. *Eur. J. Biochem.* **217**, 587–595.

Bonacker L. G., Baudner S. and Thauer R. K. (1992) Erratum: Differential expression of the two methyl-coenzyme M reductases in Methanobacterium thermoautotrophicum as described immunochemically via isoenzyme-specific antisera (European Journal of Biochemistry, Vol. 206, No. 1). *Eur. J. Biochem.* **207**, 1129.

Botz R., Pokojski H.-D., Schmitt M. and Thomm M. (1996) Carbon isotope fractionation during bacterial methanogenesis reduction. **25**, 255–262.

von Bünau R., Zirngibl C., Thauer R. K. and Klein A. (1991) Hydrogen-forming and coenzyme-F420-reducing methylene tetrahydromethanopterin dehydrogenase are genetically distinct enzymes in Methanobacterium thermoautotrophicum (Marburg). *Eur. J. Biochem.* **202**, 1205–1208.

Cao X., Bao H. and Peng Y. (2019) A kinetic model for isotopologue signatures of methane generated by biotic and abiotic CO2 methanation. *Geochim. Cosmochim. Acta* **249**, 59–75.

Chabab S., Théveneau P., Coquelet C., Corvisier J. and Paricaud P. (2020) Measurements and predictive models of high-pressure H2 solubility in brine (H2O+NaCl) for underground hydrogen storage application. *Int. J. Hydrogen Energy* **45**, 32206–32220.

Coleman M. L., Shepherd T. J., Durham J. J., Rouse J. E. and Moore G. R. (1982) Reduction of Water with Zinc for Hydrogen Isotope Analysis. *Anal. Chem.* **54**, 993–995.

Conrad R., Goodwin S. and Zeikus J. G. (1987) Hydrogen metabolism in a mildly acidic lake sediment (Knaack Lake). *FEMS Microbiol. Lett.* **45**, 243–249.

Conrad R., Phelps T. J. and Zeikus J. G. (1985) Gas metabolism evidence in support of the juxtaposition of hydrogen-producing and methanogenic bacteria in sewage sludge and lake sediments. *Appl. Environ. Microbiol.* **50**, 595–601.

Coplen T. B. (2011) Guidelines and recommended terms for expression of stable-isotope-ratio and gas-ratio measurement results. *Rapid Commun. Mass Spectrom.* **25**, 2538–2560.

Douglas P. M. J., Gonzalez Moguel R., Walter Anthony K. M., Wik M., Crill P. M., Dawson K. S., Smith D. A., Yanay E., Lloyd M. K., Stolper D. A., Eiler J. M. and Sessions A. L. (2020) Clumped Isotopes Link Older Carbon Substrates With Slower Rates of Methanogenesis in Northern Lakes. *Geophys. Res. Lett.* **47**, 1–10.

Douglas P. M. J., Stolper D. A., Eiler J. M., Sessions A. L., Lawson M., Shuai Y., Bishop A., Podlaha O. G., Ferreira A. A., Santos Neto E. V., Niemann M., Steen A. S., Huang L., Chimiak L., Valentine D. L., Fiebig J., Luhmann A. J., Seyfried W. E., Etiope G., Schoell M., Inskeep W. P., Moran J. J. and Kitchen N. (2017) Methane clumped isotopes: Progress and potential for a new isotopic tracer. *Org. Geochem.* **113**, 262–282. Available at: https://doi.org/10.1016/j.orggeochem.2017.07.016.

Douglas P. M. J., Stolper D. A., Smith D. A., Walter Anthony K. M., Paull C. K., Dallimore S., Wik M., Crill P. M., Winterdahl M., Eiler J. M. and Sessions A. L. (2016) Diverse origins of Arctic and Subarctic methane point source emissions identified with multiply-substituted isotopologues. *Geochim. Cosmochim. Acta* **188**, 163–188. Available at: http://dx.doi.org/10.1016/j.gca.2016.05.031.

Ver Eecke H. C., Butterfield D. A., Huber J. A., Lilley M. D., Olson E. J., Roe K. K., Evans L. J., Merkel A. Y., Cantin H. V. and Holden J. F. (2012) Hydrogen-limited growth of hyperthermophilic methanogens at deep-sea hydrothermal vents. *Proc. Natl. Acad. Sci. U. S. A.* **109**, 13674–13679.

Etiope G. and Sherwood Lollar B. (2013) Abiotic methane on earth. *Rev. Geophys.* **51**, 276–299.

Flores R. M., Rice C. A., Stricker G. D., Warden A. and Ellis M. S. (2008) Methanogenic pathways of coal-bed gas in the Powder River Basin, United States: The geologic factor. *Int. J. Coal Geol.* **76**, 52–75.

Fuchs G., Moll J., Scherer P. and Thauer R. (1979a) Activity, acceptor specificity and function of hydrogenase in Methanobacterium thermoautotrophicum. *Hydrog. Their Catal. Act., Struct. Funct., Work. Meet.*, 83–92.

Fuchs G., Thauer R., Ziegler H. and Stichler W. (1979b) Carbon Isotope Fractionation by

Methanobacterium thermoautotrophicum. **9**, 135–139.

Games L. M. and Hayes J. M. (1978) Methane-producing bacteria : natural frac ~ onatio ~ s of tbe stable carbon isotopes. **42**, 1295–1297.

Giunta T., Young E. D., Warr O., Kohl I., Ash J. L., Martini A., Mundle S. O. C., Rumble D., Pérez-Rodríguez I., Wasley M., LaRowe D. E., Gilbert A. and Sherwood Lollar B. (2019) Methane sources and sinks in continental sedimentary systems: New insights from paired clumped isotopologues 13CH3D and 12CH2D2. *Geochim. Cosmochim. Acta* **245**, 327–351.

Gonzalez Y., Nelson D. D., Shorter J. H., McManus J. B., Dyroff C., Formolo M., Wang D. T., Western C. M. and Ono S. (2019) Precise Measurements of 12CH2D2 by Tunable Infrared Laser Direct Absorption Spectroscopy. *Anal. Chem.* **91**, 14967–14974.

Gropp J., Iron M. A. and Halevy I. (2021) Theoretical estimates of equilibrium carbon and hydrogen isotope effects in microbial methane production and anaerobic oxidation of methane. *Geochim. Cosmochim. Acta* **295**, 237–264. Available at: https://doi.org/10.1016/j.gca.2020.10.018.

Gropp J., Jin Q. and Halevy I. (2022) Controls on the isotopic composition of microbial methane. *Sci. Adv.* **8**.

Gruen D. S., Wang D. T., Ko M., Stewart L. C., Goldhammer T., Holden J. F., Hinrichs K. and Ono S. (2018) ScienceDirect Experimental investigation on the controls of clumped isotopologue and hydrogen isotope ratios in microbial methane. **237**, 339–356.

Hattori S., Nashimoto H., Kimura H., Koba K., Yamada K., Shimizu M., Watanabe H., Yoh M. and Yoshida N. (2012) Hydrogen and carbon isotope fractionation by thermophilic hydrogenotrophic methanogens from a deep aquifer under coculture with fermenters. *Geochem. J.* **46**, 193–200.

Hayes J. M. (2001) Fractionation of carbon and hydrogen isotopes in biosynthetic processes. *Rev. Mineral. Geochemistry* **43**, 225–277.

Haynes W. M., Lide D. R. and Bruno T. J. (2016) *CRC handbook of chemistry and physics: a ready-reference book of chemical and physical data*. 97th Editi., CRC Press, Boca Raton, Florida.

Hendrickson E. L., Haydock A. K., Moore B. C., Whitman W. B. and Leigh J. A. (2007) Functionally distinct genes regulated by hydrogen limitation and growth rate in methanogenic Archaea. **2007**.

Hoehler T. M., Alperin M. J., Albert D. B. and Martens C. S. (2001) Apparent minimum free energy requirements for methanogenic Archaea and sulfate-reducing bacteria in an anoxic marine sediment. *FEMS Microbiol. Ecol.* **38**, 33–41.

Horibe Y. and Craig H. (1995) D/H fractionation in the system methane-hydrogen-water. *Geochim. Cosmochim. Acta* **59**, 5209–5217.

Horita J. (2001) Carbon isotope exchange in the system CO2-CH4 at elevated temperatures. *Geochim. Cosmochim. Acta* **65**, 1907–1919.

Horita J. and Wesolowski D. J. (1994) Horita and Wesolowski 1994. *Geochim. Cosmochim. Acta* **58**, 1–13.

Hut G. (1987) Status of Stable Isotope Reference and Intercomparison Material stored by the IAEA as per 87-01-01. *Consult. Gr. Meet. Stable Isot. Ref. Samples Geochemical Hydrol. Investig.*, 34–37. Available at: https://inis.iaea.org/collection/NCLCollectionStore/_Public/18/075/18075746.pdf.

Janssen P. H. (2010) Influence of hydrogen on rumen methane formation and fermentation balances through microbial growth kinetics and fermentation thermodynamics. *Anim. Feed*

Sci. Technol. **160**, 1–22.

Jud G., Schneider K. and Bachofen R. (1997) The role of hydrogen mass transfer for the growth kinetics of Methanobacterium thermoautotrophicum in batch and chemostat cultures. *J. Ind. Microbiol. Biotechnol.* **19**, 246–251.

Kawagucci S., Kobayashi M., Hattori S., Yamada K., Ueno Y., Takai K. and Yoshida N. (2014) Hydrogen isotope systematics among H2–H2O–CH4 during the growth of the hydrogenotrophic methanogen Methanothermobacter thermautotrophicus strain ΔH. *Geochim. Cosmochim. Acta* **142**, 601–614.

Krzycki J. A., Kenealy W. R., DeNiro M. J. and Zeikus J. G. (1987) Stable Carbon Isotope Fractionation by Methanosarcina barkeri during Methanogenesis from Acetate, Methanol, or Carbon Dioxide-Hydrogen. *Appl. Environ. Microbiol.* **53**, 2597–2599.

Kuivila K. M., Murray J. W., Devol A. H. and Novelli P. C. (1989) Methane production, sulfate reduction and competition for substrates in the sediments of Lake Washington. *Geochim. Cosmochim. Acta* **53**, 409–416.

Lin Y. S., Heuer V. B., Goldhammer T., Kellermann M. Y., Zabel M. and Hinrichs K. U. (2012) Towards constraining H2 concentration in subseafloor sediment: A proposal for combined analysis by two distinct approaches. *Geochim. Cosmochim. Acta* **77**, 186–201.

Londry K. L., Dawson K. G., Grover H. D., Summons R. E. and Bradley A. S. (2008) Stable carbon isotope fractionation between substrates and products of Methanosarcina barkeri. *Org. Geochem.* **39**, 608–621.

Lovley D. R. (1985) Minimum threshold for hydrogen metabolism in methanogenic bacteria. *Appl. Environ. Microbiol.* **49**, 1530–1531.

Macpherson J. V and Unwin P. R. (1997) Determination of the Diffusion Coefficient of

Hydrogen in Aqueous Solution Using Single and Double Potential Step Chronoamperometry at a Disk Ultramicroelectrode. *Anal. Chem.* **69**, 2063–2069.

Mariotti A., Germon J. C., Hubert P., Kaiser P., Letolle R., Tardieux A. and Tardieux P. (1981) Experimental determination of nitrogen kinetic isotope fractionation: Some principles; illustration for the denitrification and nitrification processes. *Plant Soil* **62**, 413–430.

McGinnis D. F., Kirillin G., Tang K. W., Flury S., Bodmer P., Engelhardt C., Casper P. and Grossart H. P. (2015) Enhancing surface methane fluxes from an oligotrophic lake: Exploring the microbubble hypothesis. *Environ. Sci. Technol.* **49**, 873–880.

Nguyen T. B., Topçuoğlu B. D., Holden J. F., LaRowe D. E. and Lang S. Q. (2020) Lower hydrogen flux leads to larger carbon isotopic fractionation of methane and biomarkers during hydrogenotrophic methanogenesis. *Geochim. Cosmochim. Acta* **271**, 212–226.

Novelli P. C., Scranton M. I. and Michener R. H. (1987) Hydrogen distributions in marine sediments,. *Limnol. Oceanogr.* **32**, 565–576.

Okumura T., Kawagucci S., Saito Y., Matsui Y., Takai K. and Imachi H. (2016) Hydrogen and carbon isotope systematics in hydrogenotrophic methanogenesis under H2-limited and H2-enriched conditions: implications for the origin of methane and its isotopic diagnosis. *Prog. Earth Planet. Sci.* **3**, 1–19.

Ono S., Rhim J. H., Gruen D. S., Taubner H., Kölling M. and Wegener G. (2021) Clumped isotopologue fractionation by microbial cultures performing the anaerobic oxidation of methane. *Geochim. Cosmochim. Acta* **293**, 70–85.

Ono S., Rhim J. H. and Ryberg E. C. (2022) Rate limits and isotopologue fractionations for microbial methanogenesis examined with combined pathway protein cost and isotopologue flow network models. *Geochim. Cosmochim. Acta* **325**, 296–315. Available at:

https://doi.org/10.1016/j.gca.2022.03.017.

Ono S., Wang D. T., Gruen D. S., Sherwood Lollar B., Zahniser M. S., McManus B. J. and Nelson D. D. (2014) Measurement of a doubly substituted methane isotopologue, 13CH3D, by tunable infrared laser direct absorption spectroscopy. *Anal. Chem.* **86**, 6487–6494.

Park S. H., Park C., Lee J. Y. and Lee B. (2017) A Simple Parameterization for the Rising Velocity of Bubbles in a Liquid Pool. *Nucl. Eng. Technol.* **49**, 692–699.

Pauss A., Andre G., Perrier M. and Guiot S. R. (1990) Liquid-to-Gas mass transfer in anaerobic processes: Inevitable transfer limitations of methane and hydrogen in the biomethanation process. *Appl. Environ. Microbiol.* **56**, 1636–1644.

Penning H., Plugge C. M., Galand P. E. and Conrad R. (2005) Variation of carbon isotope fractionation in hydrogenotrophic methanogenic microbial cultures and environmental samples at different energy status. *Glob. Chang. Biol.* **11**, 2103–2113.

Pihl T. D., Sharma S. and Reeve J. N. (1994) Growth phase-dependent transcription of the genes that encode the two methyl coenzyme M reductase isoenzymes and N5-methyltetrahydromethanopterin:Coenzyme M methyltransferase in Methanobacterium thermoautotrophicum ΔH. *J. Bacteriol.* **176**, 6384–6391.

Pohlman J. W., Kaneko M., Heuer V. B., Coffin R. B. and Whiticar M. (2009) Methane sources and production in the northern Cascadia margin gas hydrate system. *Earth Planet. Sci. Lett.* **287**, 504–512.

Rees C. E. (1973) A steady-state model for sulphur isotope fractionation in bacterial reduction processes. *Geochim. Cosmochim. Acta* **37**, 1141–1162.

Reeve J. N., Nölling J., Morgan R. M. and Smith D. R. (1997) Methanogenesis: Genes, Genomes, and Who's on First? *J. Bacteriol.* **179**, 5975–5986.

Robinson J. A. and Tiedje J. M. (1982) Kinetics of hydrogen consumption by rumen fluid, anaerobic digestor sludge, and sediment. *Appl. Environ. Microbiol.* **44**, 1374–1384.

Rospert S., Linder D., Ellermann J. and Thauer R. K. (1990) Two genetically distinct methyl-coenzyme M reductases in Methanobacterium thermoautotrophicum strain Marburg and ΔH. *Eur. J. Biochem.* **194**, 871–877.

Scheller S., Goenrich M., Thauer R. K. and Jaun B. (2013) Methyl-Coenzyme M Reductase from Methanogenic Archaea: Isotope E ff ects on the Formation and Anaerobic Oxidation of Methane.

Schoell M. (1988) Multiple origins of methane in the Earth. *Chem. Geol.* **71**, 1–10.

Sherwood Lollar B., Lacrampe-Couloume G., Voglesonger K., Onstott T. C., Pratt L. M. and Slater G. F. (2008) Isotopic signatures of CH4 and higher hydrocarbon gases from Precambrian Shield sites: A model for abiogenic polymerization of hydrocarbons. *Geochim. Cosmochim. Acta* **72**, 4778–4795.

Sherwood Lollar B., Westgate T. D., Ward J. A., Slater G. F. and Lacrampe-Couloume G. (2002) Abiogenic formation of alkanes in the earth's crust as a minor source for global hydrocarbon reservoirs. *Nature* **416**, 522–524.

Smolenski W. J. and Robinson J. A. (1988) In situ rumen hydrogen concentrations in steers fed eight times daily, measured using a mercury reduction detector. *FEMS Microbiol. Lett.* **53**, 95–100.

Stewart L. C., Llewellyn J. G., Butterfield D. A., Lilley M. D. and Holden J. F. (2016) Hydrogen and thiosulfate limits for growth of a thermophilic, autotrophic Desulfurobacterium species from a deep-sea hydrothermal vent. *Environ. Microbiol. Rep.* **8**, 196–200.

Stolper D. A., Martini A. M., Clog M., Douglas P. M., Shusta S. S., Valentine D. L., Sessions A.

L. and Eiler J. M. (2015) Distinguishing and understanding thermogenic and biogenic sources of methane using multiply substituted isotopologues. *Geochim. Cosmochim. Acta* **161**, 219–247.

Stolper D. A., Sessions A. L., Ferreira A. A., Santos Neto E. V., Schimmelmann A., Shusta S. S., Valentine D. L. and Eiler J. M. (2014) Combined 13C-D and D-D clumping in methane: Methods and preliminary results. *Geochim. Cosmochim. Acta* **126**, 169–191. Available at: http://dx.doi.org/10.1016/j.gca.2013.10.045.

Teramoto M., Fujita S., Kataoka M. and Hashimoto K. (1970) Effect of Bubble Size on the Selectivity of Consecutive Gas-Liquid Reactions. In *Meeting of the Society of the Chemical Engineers (Japan)* pp. 79–82.

Thauer R. K. (2011) Anaerobic oxidation of methane with sulfate: On the reversibility of the reactions that are catalyzed by enzymes also involved in methanogenesis from CO2. *Curr. Opin. Microbiol.* **14**, 292–299.

Thauer R. K., Kaster A. K., Seedorf H., Buckel W. and Hedderich R. (2008) Methanogenic archaea: Ecologically relevant differences in energy conservation. *Nat. Rev. Microbiol.* **6**, 579–591.

Topçuoğlu B. D., Meydan C., Orellana R. and Holden J. F. (2018) Formate hydrogenlyase and formate secretion ameliorate H 2 inhibition in the hyperthermophilic archaeon Thermococcus paralvinellae. *Environ. Microbiol.* **20**, 949–957.

Topçuoğlu B., Meydan C., Nguyen T., Lang S. and Holden J. F. (2019) Growth Kinetics, Carbon Isotope Fractionation, and Gene Expression in the Hyperthermophile Methanocaldococcus jannaschii during Hydrogen-Limited Growth and Interspecies Hydrogen Transfer Begüm. **85**, 1–14.

Turner A. C., Korol R., Eldridge D. L., Bill M., Conrad M. E., Miller T. F. and Stolper D. A. (2021) Experimental and theoretical determinations of hydrogen isotopic equilibrium in the system CH4–H2–H2O from 3 to 200 °C. *Geochim. Cosmochim. Acta* **314**, 223–269. Available at: https://doi.org/10.1016/j.gca.2021.04.026.

Valentine D. L., Chidthaisong A., Rice A., Reeburgh W. S. and Tyler S. C. (2004) Carbon and hydrogen isotope fractionation by moderately thermophilic methanogens. *Geochim. Cosmochim. Acta* **68**, 1571–1590.

Wang D. T., Gruen D. S., Lollar B. S., Hinrichs K.-U., Stewart L. C., Holden J. F., Hristov A. N., Pohlman J. W., Morrill P. L., Könneke M., Delwiche K. B., Reeves E. P., Sutcliffe C. N., Ritter D. J., Seewald J. S., McIntosh J. C., Hemond H. F., Kubo M. D., Cardace D., Hoehler T. M. and Ono S. (2015) Nonequilibrium clumped isotope signals in microbial methane. *Science (80-.).* **348**, 428–431.

Wang D. T., Welander P. V. and Ono S. (2016) Fractionation of the methane isotopologues 13CH4, 12CH3D, and 13CH3D during aerobic oxidation of methane by Methylococcus capsulatus (Bath). *Geochim. Cosmochim. Acta* **192**, 186–202. Available at: http://dx.doi.org/10.1016/j.gca.2016.07.031.

Welhan J. A. and Lupton J. E. (1987) Light hydrocarbon gases in Guaymas Basin hydrothermal fluids: thermogenic versus abiogenic origin. *Am. Assoc. Pet. Geol. Bull.* **71**, 215–223.

Whiticar M. J. (1990) A geochemial perspective of natural gas and atmospheric methane. *Org. Geochem.* **16**, 531–547.

Whiticar M. J. (1999) Carbon and hydrogen isotope systematics of bacterial formation and oxidation of methane. *Chem. Geol.* **161**, 291–314.

Wolfe R. S. (2011) *Techniques for cultivating methanogens*. 1st ed., Elsevier Inc.

Yoshioka H., Sakata S. and Kamagata Y. (2008) Hydrogen isotope fractionation by Methanothermobacter thermoautotrophicus in coculture and pure culture conditions. *Geochim. Cosmochim. Acta* **72**, 2687–2694.

Young E. D., Kohl I. E., Lollar B. S., Etiope G., Rumble D., Li (李姝宁) S., Haghnegahdar M. A., Schauble E. A., McCain K. A., Foustoukos D. I., Sutclife C., Warr O., Ballentine C. J., Onstott T. C., Hosgormez H., Neubeck A., Marques J. M., Pérez-Rodríguez I., Rowe A. R., LaRowe D. E., Magnabosco C., Yeung L. Y., Ash J. L. and Bryndzia L. T. (2017) The relative abundances of resolved l2CH2D2 and 13CH3D and mechanisms controlling isotopic bond ordering in abiotic and biotic methane gases. *Geochim. Cosmochim. Acta* **203**, 235–264.

Young E. D., Rumble D., Freedman P. and Mills M. (2016) A large-radius high-mass-resolution multiple-collector isotope ratio mass spectrometer for analysis of rare isotopologues of O2, N2, CH4 and other gases. *Int. J. Mass Spectrom.* **401**, 1–10.

Zhang N., Snyder G. T., Lin M., Nakagawa M., Gilbert A., Yoshida N., Matsumoto R. and Sekine Y. (2021) Doubly substituted isotopologues of methane hydrate (13CH3D and 12CH2D2): Implications for methane clumped isotope effects, source apportionments and global hydrate reservoirs. *Geochim. Cosmochim. Acta* **315**, 127–151. Available at: https://doi.org/10.1016/j.gca.2021.08.027.

Tables

Table 1. Summary of experiments.

Experiment	Organism	Temp. (°C)	xH_2 (%)	System
B.82	*Methanocaldococcus bathoardescens*	82	80	Batch
F.82.80	*Methanocaldococcus bathoardescens*	82	80	Fed-batch
F.82.25	*Methanocaldococcus bathoardescens*	82	25	Fed-batch
F.60.80	*Methanocaldococcus bathoardescens*	60	80	Fed-batch
F65.20	*Methanothermobacter thermautotrophicus* (ΔH)	65	20	Fed-batch
F.65.5	*Methanothermobacter thermautotrophicus* (ΔH)	65	5→1.6	Fed-batch

Table 2. Parameters used for model calculation described in 2.3.7.

Parameter	Values used (range)	Sources/Notes
r_b	0.05 cm (0.025 to 0.1 cm)	Teramoto *et al.* (1970)
D	5×10^{-5} cm²/sec	Macpherson and Unwin (1997)
A_b	200 cm²	Calculated for a gas flow rate of 200 mL/min, medium height of 20 cm, and bubble radius of 0.05 cm; Park et al. (2017)
A_h	177 cm²	Calculated for a known reactor I.D. = 15 cm

Table 3. Results for batch culture experiment (Experiment B.82). *Methanocaldococcus bathoardescens* was grown at 82 °C on 80% H_2. The headspace pressure decreased, as 5 moles of gas were consumed to produce 1 mole of gas (Eqn. 7). Therefore, volumes (in mL) of H_2, CO_2, and CH_4 were calculated assuming 4:1:1 reaction stoichiometries and mixing ratios for H_2: CO_2:CH_4 measure by GC (Table 3; Supplementary Material, Figure S1).

Time (h)	cells/mL	H_2 (mL)†	CO_2 (mL)†	CH_4 (mL)†	$\delta^{13}C_{CO2}$ (‰)	$\delta^{13}C_{CH4}$ (‰)	δD_{H2O} (‰)	δD_{CH4} (‰)	$\Delta^{13}CH_3D$ (‰)	CI
0.0	-	288.24	47.35	0.13	-34.9	-	-45.4	-	-	-
1.0	1.1E+6	281.61	50.49	0.53	-	-	-46.9	-	-	-
1.9	5.5E+6	258.65	44.57	6.83	-31.4	-	-	-	-	-
3.0	3.7E+7	125.88	13.33	36.98	-14.3	-47.1	-46.5	-407.6	0.48	0.20
4.0	3.6E+7	78.29	4.55	48.45	-25.1	-39.5	-	-409.6	0.38	0.19
5.0	7.4E+7	68.78	2.84	50.48	-	-	-	-	-	-
6.0	7.1E+7	35.52	2.60	58.35	-22.0	-	-	-	-	-
6.9	4.3E+7	53.28	2.11	53.90	-	-38.8	-46.0	-413.3	0.32	0.26

† volume of gas calculated based on mixing ratios and expected headspace pressure at the time of measurement; – values not determined; CI is the 95% confidence interval in permil (‰).

Table 4. Results for fed-batch experiments. *Methanocaldococcus bathoardescens* was grown at 82 °C and 80% H_2 (F.82.80); at 60 °C and 80% H_2 (F.60.80); and at 82 °C and 25% H_2 (F.82.25).

Experiment	Time (h)	cells/mL	H_2 (%)	CO_2 (%)	CH_4 (%)	MPR (mol/h)	csMPR (pmol/cell/h)	$\delta^{13}C_{CO2}$ (‰)	$\delta^{13}C_{CH4}$ (‰)	CI	$\alpha_{CH4\ CO2}$	δD_{H2O} (‰)	δD_{CH4} (‰)	CI	$\alpha_{CH4\ H2O}$	$\Delta^{13}CH_3D$ (‰)	CI
F.82.80	0.0	6.8×10^5	79.8	19.9	0.08	4.1×10^{-4}	0.34	-39.9	-	-	*	-53.7	-	-	*	-	-
F.82.80	0.0	-	80.7	19.5	1.78	8.1×10^{-3}	-	-	-	-	*	-	-	-	*	-	-
F.82.80	1.1	5.2×10^6	-	-	-	-	-	-	-	-	*	-	-	-	*	-	-
F.82.80	1.5	-	76.6	20.0	3.75	1.6×10^{-2}	-	-21.3	-68.16	0.11	0.952	-53.8	-362.63	0.09	0.674	1.25	0.48
F.82.80	2.2	2.0×10^7	77.2	19.8	4.03	1.7×10^{-2}	0.48	-25.8	-76.62	0.09	0.948	-	-336.86	0.07	*	0.38	0.43
F.82.80	2.5	2.8×10^7	77.9	18.5	4.02	1.7×10^{-2}	0.34	-	-74.27	0.06	*	-	-331.75	0.08	*	-0.17	0.49
F.82.80	3.0	3.2×10^7	78.0	18.6	4.09	1.7×10^{-2}	0.30	-	-80.22	0.04	*	-	-333.61	0.04	*	0.07	0.83
F.82.80	3.5	4.1×10^7	-	-	-	-	-	-	-	-	*	-	-	-	*	-	-
F.82.80	3.7	4.5×10^7	77.0	19.2	3.92	1.7×10^{-2}	0.21	-	-77.90	0.06	*	-	-331.81	0.06	*	-0.29	0.47
F.82.80	22.0	-	-	-	-	-	-	-	-69.09	0.14	*	-54.0	-329.88	0.08	0.708	-0.01	0.27
F.60.80	0.0	5.8×10^6	75.5	21.9	0.06	3.1×10^{-4}	0.03	-	-	-	*	-	-	-	*	-	-
F.60.80	1.5	1.7×10^7	73.9	22.3	0.47	2.5×10^{-3}	0.08	-38.8	-56.42	-	0.982	-	-305.00	-	*	2.06	-
F.60.80	1.8	-	75.3	22.1	0.50	2.6×10^{-3}	-	-	-	-	*	-	-	-	*	-	-
F.60.80	2.8	1.4×10^7	73.1	22.4	1.38	7.0×10^{-3}	0.29	-	-	-	*	-	-	-	*	-	-
F.60.80	3.3	-	75.1	22.2	1.90	9.2×10^{-3}	-	-36.8	-60.14	0.10	0.976	-	-364.48	0.17	*	1.52	0.58
F.60.80	3.8	2.4×10^7	72.5	21.1	2.98	1.4×10^{-2}	0.33	-	-	-	*	-	-	-	*	-	-
F.60.80	5.6	1.3×10^8	74.0	21.1	4.14	1.8×10^{-2}	0.08	-	-	-	*	-	-	-	*	-	-
F.60.80	6.4	-	74.5	21.0	3.94	1.7×10^{-2}	-	-33.6	-68.88	0.11	0.964	-	-321.41	0.06	*	0.80	0.28
F.60.80	6.7	1.1×10^8	71.7	21.3	3.64	1.7×10^{-2}	0.08	-	-	-	*	-	-	-	*	-	-
F.60.80	7.8	1.4×10^8	73.9	21.4	3.91	1.7×10^{-2}	0.07	-	-	-	*	-	-	-	*	-	-
F.60.80	8.9	1.9×10^8	71.7	21.2	3.7	1.7×10^{-2}	0.05	-	-	-	*	-	-	-	*	-	-
F.60.80	9.4	-	73.7	21.6	4.07	1.8×10^{-2}	-	-32.6	-67.47	0.04	0.964	-	-314.58	0.04	*	0.06	0.17
F.82.25	0.0	1.0×10^6	23.1	21.8	BDL	-	-	-	-	-	*	-	-	-	*	-	-
F.82.25	0.2	-	23.1	21.9	0.03	1.6×10^{-2}	-	-14.0	-50.75	0.10	0.963	-40.4	-358.78	0.04	0.668	1.15	0.42
F.82.25	0.5	4.4×10^6	22.8	23.6	0.41	2.1×10^{-3}	0.27	-	-	-	*	-	-	-	*	-	-
F.82.25	1.7	1.3×10^7	22.6	22.9	1.30	5.8×10^{-3}	0.25	-	-	-	*	-39.9	-	-	*	-	-
F.82.25	2.3	9.1×10^6	22.5	23.8	1.39	6.2×10^{-3}	0.38	-	-	-	*	-	-	-	*	-	-
F.82.25	2.8	9.6×10^6	22.4	23.5	1.53	6.7×10^{-3}	0.39	-	-	-	*	-40.1	-	-	*	-	-
F.82.25	3.6	2.1×10^7	22.4	23.8	1.56	6.8×10^{-3}	0.18	-	-	-	*	-	-	-	*	-	-
F.82.25	4.4	7.4×10^6	22.5	23.9	1.47	6.5×10^{-3}	0.49	-	-	-	*	-40.0	-	-	*	-	-
F.82.25	4.9	2.4×10^7	22.4	24.2	1.57	6.8×10^{-3}	0.16	-	-	-	*	-	-	-	*	-	-
F.82.25	5.2	2.8×10^7	16.7	22.8	1.41	7.9×10^{-3}	0.16	-	-	-	*	-	-	-	*	-	-
F.82.25	19.0	2.0×10^8	22.6	23.6	1.69	7.2×10^{-3}	0.02	-	-	-	*	-	-	-	*	-	-
F.82.25	22.5	1.0×10^8	22.6	23.9	1.51	6.6×10^{-3}	0.04	-	-	-	*	-	-	-	*	-	-
F.82.25	24.5	9.6×10^7	22.6	23.3	1.57	6.8×10^{-3}	0.04	-	-	-	*	-	-	-	*	-	-
F.82.25	24.7	-	22.4	23.9	1.82	7.7×10^{-3}	-	-12.0	-70.79	0.05	0.941	-	-328.61	0.09	*	-0.78	0.73
F.82.25	25.8	8.1×10^7	22.5	23.0	1.65	7.1×10^{-3}	0.05	-	-	-	*	-	-	-	*	-	-
F.82.25	26.8	1.0×10^8	22.2	2.0	2.05	8.5×10^{-3}	0.05	-	-	-	*	-	-	-	*	-	-
F.82.25	43.7	1.5×10^8	21.6	23.8	2.82	1.1×10^{-2}	0.04	-	-	-	*	-	-	-	*	-	-
F.82.25	44.4	-	21.6	24.8	2.71	1.0×10^{-2}	-	-9.9	-67.78	0.03	0.941	-	-327.72	0.05	*	-0.65	0.36
F.82.25	45.2	-	21.7	23.3	2.89	1.1×10^{-2}	-	-10.3	-	-	*	-	-	-	*	-	-
F.82.25	52.5	2.1×10^8	21.2	24.9	2.62	1.0×10^{-2}	0.03	-	-	-	*	-	-	-	*	-	-

– values not determined; * not applicable; CI is the 95% confidence interval in permil (‰).

Table 5. Results for fed-batch experiments. *Methanothermobacter thermautotrophicus* was grown at 65 °C and 20% H_2 (Experiment F.65.20) and at 65 °C and 5–1.6% H_2 (Experiment F.65.5).

Experiment	Time (h)	cells/mL	H_2 (%)	CO_2 (%)	CH_4 (%)	MPR (mol/h)	csMPR (pmol/cell/h)	$\delta 13C_{CO2}$ (‰)	$\delta^{13}C_{DIC}$ (‰)	$\alpha_{CO2\text{-}DIC}$	$\delta^{13}C_{CH4}$ (‰)	CI	$\alpha_{CH4\text{-}CO2}$	δD_{H2O} (‰)	δD_{CH4} (‰)	CI	$\alpha_{CH4\text{-}H2O}$	$\Delta^{13}CH_3D$ (‰)	CI
F.65.20	0.0	2.3×10^5	21.6	18.7	0.01	4.2×10^{-5}	0.100	-15.3	-11.7	0.9963	-	-	*	-45.5	-	-	*	-	-
F.65.20	2.2	4.8×10^5	21.2	19.4	0.03	1.4×10^{-4}	0.161	-	-	*	-	-	*	-	-	-	*	-	-
F.65.20	5.8	1.2×10^6	21.1	19.3	0.10	4.6×10^{-4}	0.217	-	-	*	-	-	*	-	-	-	*	-	-
F.65.20	11.7	4.8×10^6	19.9	19.3	0.44	2.0×10^{-3}	0.241	-14.9	-10.5	0.9956	-48.35	0.15	0.966	-45.5	-361.81	0.62	0.669	0.33	0.57
F.65.20	22.8	4.8×10^7	19.5	17.9	0.69	3.1×10^{-3}	0.036	-14.9	-9.7	0.9947	-57.04	0.19	0.957	-	-363.27	0.27	0.667	-2.03	0.50
F.65.20	25.7	6.9×10^7	19.5	18.1	0.70	3.1×10^{-3}	0.025	-	-	*	-	-	*	-	-	-	*	-	-
F.65.20	28.1	7.7×10^7	19.5	18.1	0.70	3.1×10^{-3}	0.023	-	-9.7	*	-	-	*	-45.5	-	-	*	-	-
F.65.20	33.3	1.1×10^8	19.5	18.1	0.71	3.2×10^{-3}	0.016	-14.0	-	*	-	-	*	-	-	-	*	-	-
F.65.20	47.2	1.8×10^8	19.3	18.7	0.72	3.3×10^{-3}	0.010	-13.9	-9.4	0.9955	-62.12	0.16	0.951	-	-347.04	0.24	0.684	-1.28	0.87
F.65.20	53.2	2.1×10^8	19.2	19.3	0.74	3.3×10^{-3}	0.009	-13.6	-9.5	0.9958	-	-	*	-	-	-	*	-	-
F.65.20	70.2	2.9×10^8	19.3	18.1	0.76	3.4×10^{-3}	0.007	-	-	*	-	-	*	-	-	-	*	-	-
F.65.20	77.0	2.7×10^8	19.3	19.0	0.76	3.4×10^{-3}	0.007	-13.6	-9.4	0.9957	-62.94	0.21	0.950	-	-352.35	0.37	0.679	-1.09	0.65
F.65.20	94.9	3.1×10^8	19.4	18.8	0.78	3.5×10^{-3}	0.006	-	-	*	-	-	*	-	-	-	*	-	-
F.65.20	101.9	4.5×10^8	19.0	18.9	0.81	3.6×10^{-3}	0.005	-13.8	-9.6	0.9958	-63.30	0.34	0.950	-	-351.36	0.60	0.677	-1.91	0.54
F.65.20	102.4	3.9×10^8	19.2	19.5	0.80	3.6×10^{-3}	0.005	-	-	*	-	-	*	-	-	-	*	-	-
F.65.20	119.2	4.1×10^8	18.9	19.5	0.80	3.6×10^{-3}	0.005	-	-	*	-	-	*	-	-	-	*	-	-
F.65.20	122.8	-	-	-	-	-	-	-	-	*	-	-	*	-41.4	-	-	*	-	-
F.65.5	0.0	2.8×10^5	4.9	20.3	0.01	5.3×10^{-5}	0.105	-15.7	-11.4	0.9957	-	-	-	-44.9	-	-	*	-	-
F.65.5	1.7	4.7×10^5	4.8	19.6	0.04	1.8×10^{-4}	0.213	-	-	*	-	-	-	-	-	-	*	-	-
F.65.5	4.9	1.1×10^6	4.5	20.7	0.09	4.8×10^{-4}	0.256	-	-	*	-	-	-	-	-	-	*	-	-
F.65.5	9.4	2.5×10^6	4.4	19.7	0.1	7.1×10^{-4}	0.158	-	-	*	-57.96	0.23	0.957	-	-364.10	0.39	0.666	1.28	0.98
F.65.5	10.5	-	-	-	-	-	-	-15.5	-11.4	0.9959	-	-	-	-	-	-	*	-	-
F.65.5	11.8	5.9×10^6	4.4	19.6	0.14	7.2×10^{-4}	0.069	-	-	*	-	-	-	-	-	-	*	-	-
F.65.5	21.9	1.4×10^7	4.3	20.5	0.16	8.0×10^{-4}	0.032	-	-	*	-67.03	0.17	0.947	-	-371.68	0.23	0.658	-2.06	0.47
F.65.5	23.3	-	-	-	-	-	-	-15.2	-10.9	0.9956	-	-	-	-45.5	-	-	*	-	-
F.65.5	27.5	2.5×10^7	4.4	19.3	0.16	7.8×10^{-4}	0.017	-	-	*	-	-	-	-	-	-	*	-	-
F.65.5	30.3	2.7×10^7	4.4	19.0	0.16	7.8×10^{-4}	0.016	-	-11.0	*	-	-	-	-	-	-	*	-	-
F.65.5	46.0	5.1×10^7	4.3	20.6	0.17	8.4×10^{-4}	0.009	-	-	*	-	-	-	-	-	-	*	-	-
F.65.5	54.0	5.8×10^7	4.3	19.5	0.17	8.6×10^{-4}	0.008	-15.3	-11.3	0.9959	-70.55	0.32	0.944	-45.2	-368.40	0.42	0.661	-2.92	0.84
F.65.5	72.5	6.6×10^7	1.6	20.3	0.06	2.5×10^{-4}	0.002	-15.6	-11.5	0.9958	-77.54	0.20	0.937	-	-365.27	0.32	0.665	-2.52	0.46
F.65.5	95.3	7.2×10^7	1.6	20.1	0.06	2.6×10^{-4}	0.002	-	-	*	-76.93	0.17	0.938	-	-370.04	0.25	0.659	-4.13	0.46
F.65.5	97.3	-	-	-	-	-	-	-15.6	-11.4	0.9958	-	-	-	-	-	-	*	-	-
F.65.5	119.4	7.0×10^7	1.5	21.4	0.06	2.6×10^{-4}	0.002	-	-	*	-	-	-	-	-	-	*	-	-
F.65.5	143.2	7.7×10^7	1.5	20.8	0.06	2.6×10^{-4}	0.002	-	-	*	-	-	-	-43.5	-	-	*	-	-

– values not determined; * not applicable; CI is the 95% confidence interval in permil (‰)

Figure Captions

Figure 1. Schematic diagram of the fed-batch culturing system

Figure 2. Schematic overview of the biochemical pathway involved in hydrogenotrophic methanogenesis and isotopologue flow network model scenarios in this study. (A) Overview of the biochemical pathway and enzymes associated with each step. Grey bubbles represent pools of cellular carbon, grouped into those with the same redox state. The four H-addition steps are labeled with numbers. Fd_{red}, reduced ferredoxin; Fd_{ox}, oxidized ferredoxin; MFR, methanofuran; H_4MPT, tetrahydromethanopterin; F_{420}, coenzyme F_{420}; CoM-HS, coenzyme M; CoB-SH, coenzyme B; Ftr, formyl-MFR: H_4MPT formyltransferase; Mch, N^5,N^{10}-methenyl- H_4MPT cyclohydrolase; Mtd, F_{420}-dependent N^5,N^{10}-methylene-H_4MPT dehydrogenase; Hmd, H_2-forming N^5,N^{10}-methylene-H_4MPT dehydrogenase; Mer, F_{420}-dependent N^5,N^{10}-methylene-H_4MPT reductase; Mtr, N^5-methyl- H_4MPT:CoM methyltransferase; Mcr, methyl CoM reductase. Panels B, C and D show the three model scenarios tested in this study. $K_{m,n}$ values are effective half-saturation constants used to assign reversibilities to H-addition steps. (B) Equilibrium end-member scenario has a $K_{m,n}$ value of 10^4 M for all four H-addition steps (n=1–4). (C) Uniform reversibility scenario has a $K_{m,n}$ value of 10^{-8} M for all four H-addition steps (n=1–4). (D) In differential reversibility scenario, the last step is less reversible compared to the preceding three H-addition steps ($K_{m,1–3} = 5 \times 10^{-5}$ M; $K_{m,4} = 10^{-8}$ M for the last step).

Figure 3. Summary of fed-batch experiment results of this study. Each column (columns A–E) shows the result for each fed-batch experiment. The experiment names and conditions can be found at the top of each column. Each row (rows 1–6) shows a type of data. Modeled values of dissolved hydrogen concentration or $[H_2]$ (µM; row 1), cell density (cells/mL; row 2), methane production rate or MPR (µmol/sec; row 3), carbon isotope fractionation factor or $^{13}\alpha$ (row 4), hydrogen isotope

fractionation factor or $^{2}\alpha$ (row 5), and methane clumped isotope abundance or $\Delta^{13}CH_3D$ (‰; row 6). For the [H_2] model results (row 1), open squares represent maximum [H_2] values expected at equilibrium with the dry headspace mixing ratios (xH_2). Filled circles represent [H_2] values expected at equilibrium that are corrected for saturation water vapor pressure (pH_2O_{sat}) at respective temperatures (0.51 bars at 82 °C, 0.25 bars at 65 °C and 0.20 bars at 60 °C). Triangles represent pH_2O_{sat}-corrected [H_2] values expected during methane production with two different k_La values: 700 h^{-1} (down-pointing yellow triangles) and 350 h^{-1} (up-pointing blue triangles). Refer to 2.3.7 for details. Grey horizontal lines in rows 4–6 represent the equilibrium $^{13}\alpha$, $^{2}\alpha$ and $\Delta^{13}CH_3D$ values expected at respective experimental temperatures. Grey vertical lines in column 5 for F.65.5 indicate the time at which xH_2 was switched from 5% to 1.6%. Each panel shares the y-axis with the panel to its left unless new axis tick marks are introduced. Note that the x-axes (incubation time) vary across experiments (across different columns).

Figure 4. Changes in carbon ($^{13}\alpha$) and hydrogen ($^{2}\alpha$) isotope fractionation factors and $\Delta^{13}CH_3D$ values during hydrogenotrophic methanogenesis. Panels A, B and C, respectively, show $^{13}\alpha$, $^{2}\alpha$ and $\Delta^{13}CH_3D$ values measured in this study and reported in the literature, as a function of H_2 partial pressure (pH_2) in the supply gas. Color triangle and diamond symbols represent data from this study. Grey circles in panels A and B represent the $^{13}\alpha$ and $^{2}\alpha$ values from the literature (Games and Hayes, 1978; Fuchs et al., 1979b; Belyaev et al., 1983; Balabane et al., 1987; Krzycki et al., 1987; Botz et al., 1996; Valentine et al., 2004; Yoshioka et al., 2008; Hattori et al., 2012; Kawagucci et al., 2014; Okumura et al., 2016). Grey symbols in panel C represent the $\Delta^{13}CH_3D$ values obtained from pure culture hydrogenotrophic methanogenesis experiments in closed systems (Stolper et al., 2015; Wang et al., 2015; Young et al., 2017; Gruen et al., 2018; Giunta et al., 2019). Filled and open circles represent thermophilic and mesophilic temperatures,

respectively. Dashed lines represent the $^{13}\alpha$, $^{2}\alpha$ and $\Delta^{13}CH_3D$ values expected at equilibrium at temperatures indicated in the legend.

Figure 5. Modeled carbon ($\delta^{13}C$) and hydrogen (δD) isotope and clumped isotopologue compositions ($\Delta^{13}CH_3D$) of methane produced via hydrogenotrophic methanogenesis. Panel A, B, and C show the modeled $\delta^{13}C$, δD and $\Delta^{13}CH_3D$ values of methane, respectively. Dotted lines (yellow) show the model results at 82 °C for the equilibrium end-member scenario ($K_{m,1–4} = 10^4$ M). Dashed lines (red) show the results for the uniform reversibility scenario ($K_{m,1–4} = 10^{-8}$ M). Solid lines (blue) show a differential reversibility scenario, where the last H-addition step is less reversible compared to the preceding three H-addition steps ($K_{m,1–3} = 5\times10^{-5}$ M, $K_{m,4} = 10^{-8}$ M).

Figure 6. Carbon ($^{13}\alpha$) and hydrogen ($^{2}\alpha$) isotope fractionation factors and $\Delta^{13}CH_3D$ values as a function of modeled dissolved H_2 concentration, [H_2]. Panel A shows the typical ranges of [H_2] observed in natural environments and culture studies. The [H_2] ranges for batch cultures studies were calculated assuming 1–2 bars of 80% H_2 in the headspace at 25 °C. Note that the pH_2 values for batch co-cultures (Okumura et al., 2016) are based on headspace mixing ratios and that [H_2] in the co-cultures are likely higher than $[H_2]^{eq}$ expected in equilibrium with pH_2. Panels B, C and D compare the result of the isotopologue flow network model and experimental data from this study. Color symbols and corresponding experiment names are shown in the legend. Horizontal dashed lines represent the $^{13}\alpha$, $^{2}\alpha$ and $\Delta^{13}CH_3D$ values expected at equilibrium at corresponding temperatures as shown in the legend. Solid lines are modeled trajectories of $^{13}\alpha$, $^{2}\alpha$ and $\Delta^{13}CH_3D$ for the differential reversibility scenario based on the isotopologue flow network model results (see Figure 5). The horizontal error bars on triangle and diamond symbols (data from this study) show a range of [H_2] estimates under experimental conditions. Maximum [H_2] is the value expected when the medium is saturated with respect to headspace H_2 mixing ratio (x_{H2}) without

considering water vapor pressure at corresponding incubation temperatures (pH_2O_{sat}) or biological consumption of H_2. The minimum [H_2] is the value calculated using Eqn. 13, which considers both the effect of pH_2O_{sat} and H_2 consumption by methanogens during experiments based on methane production rate (MPR). The horizontal error bars on grey and light blue symbols (environmental data; microbial and non-microbial methane, respectively) show the range of [H_2] values measured at the field site or estimated for the general type of environment (e.g., 2–60 nM for marine sediments; 0.1–50 μM for cow rumen).

Figures

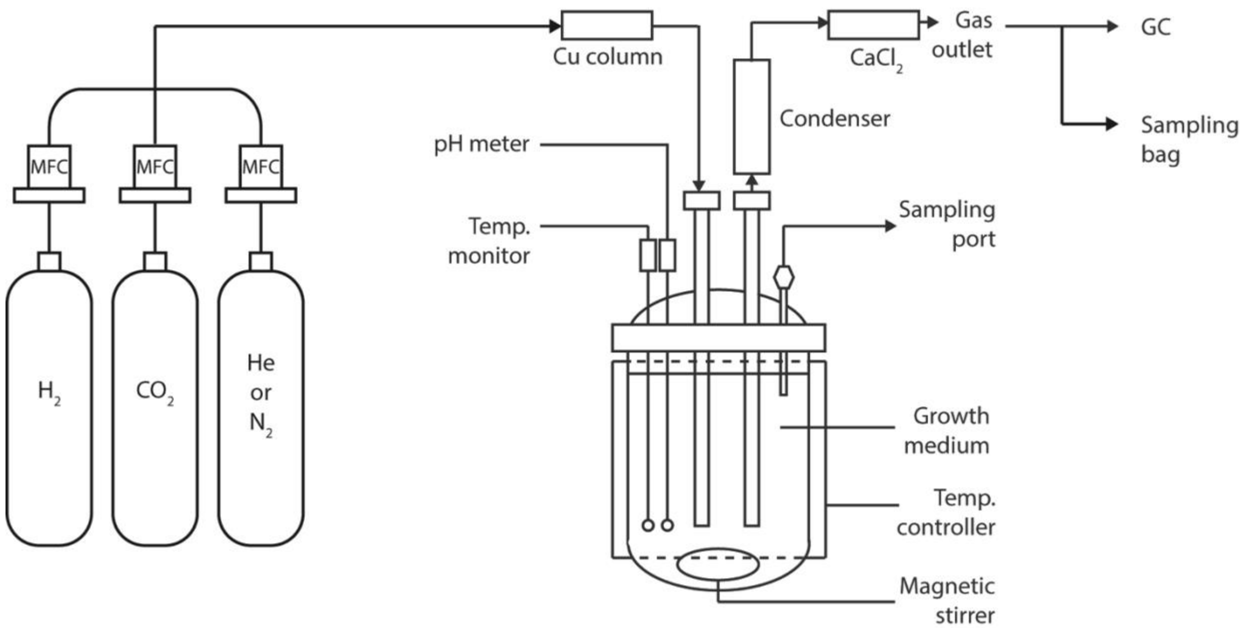

Figure 1

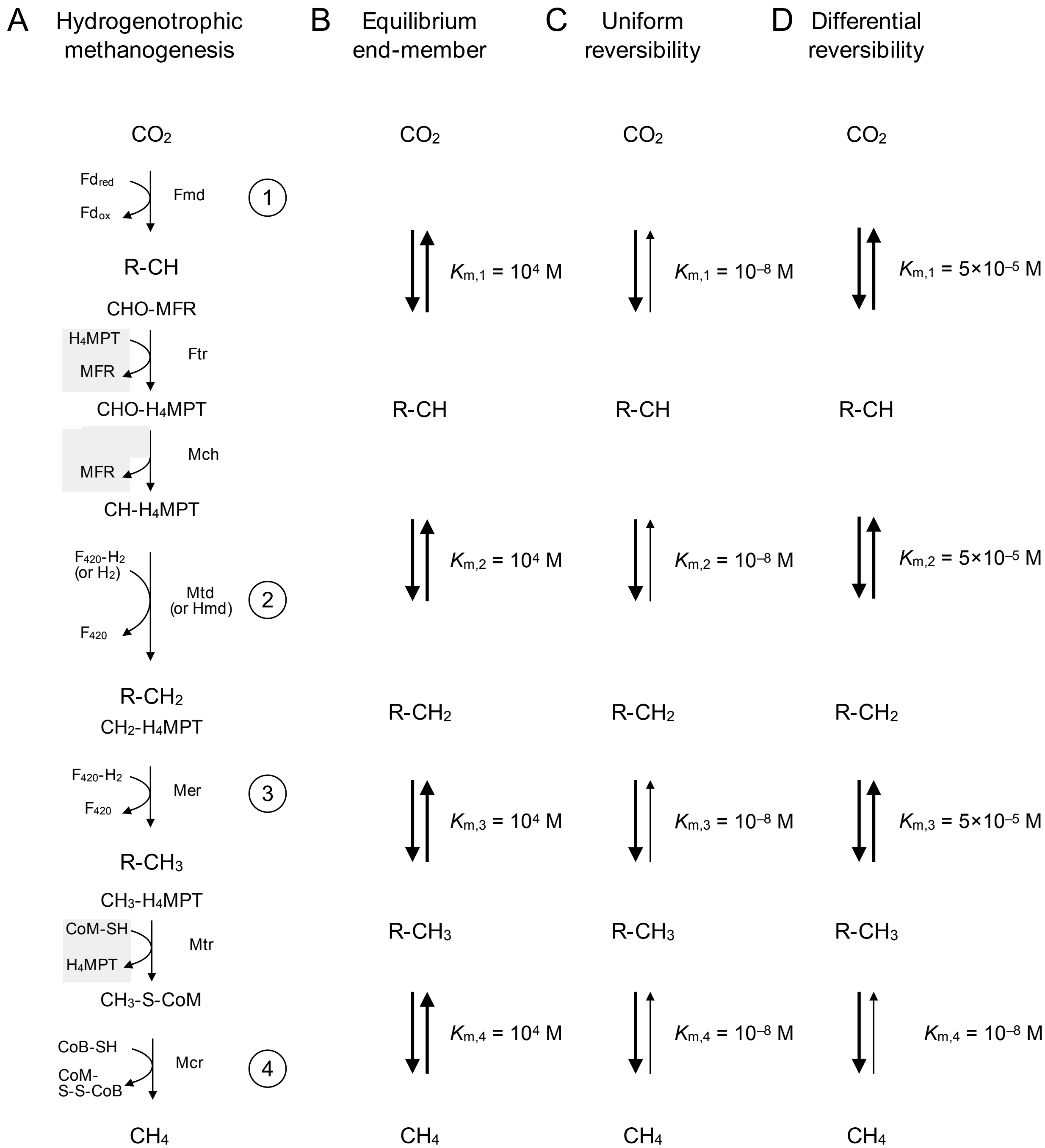
A Hydrogenotrophic methanogenesis
B Equilibrium end-member
C Uniform reversibility
D Differential reversibility
CO2
Fdred
Fdox
Fmd
1
R-CH
CHO-MFR
H4MPT
MFR
Ftr
CHO-H4MPT
MFR
Mch
CH-H4MPT
F420-H2
(or H2)
F420
Mtd
(or Hmd)
2
R-CH2
CH2-H4MPT
F420-H2
F420
Mer
3
R-CH3
CH3-H4MPT
CoM-SH
H4MPT
Mtr
CH3-S-CoM
CoB-SH
CoM-
S-S-CoB
Mcr
4
CH4
Km,1 = 10^4 M
Km,2 = 10^4 M
Km,3 = 10^4 M
Km,4 = 10^4 M
Km,1 = 10^-8 M
Km,2 = 10^-8 M
Km,3 = 10^-8 M
Km,4 = 10^-8 M
Km,1 = 5×10^-5 M
Km,2 = 5×10^-5 M
Km,3 = 5×10^-5 M
Km,4 = 10^-8 M

Figure 2

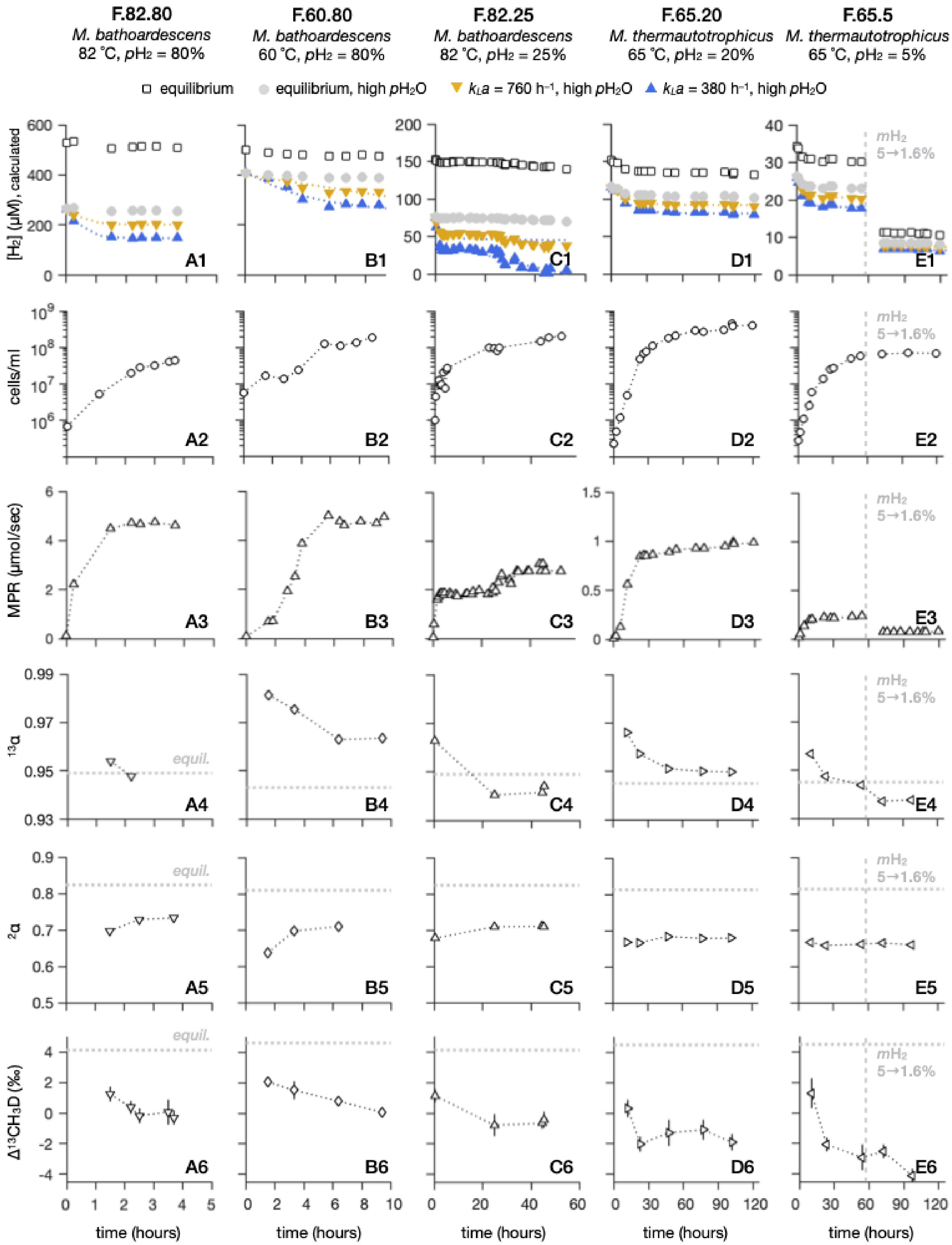

1089
1090
1091 **Figure 3**

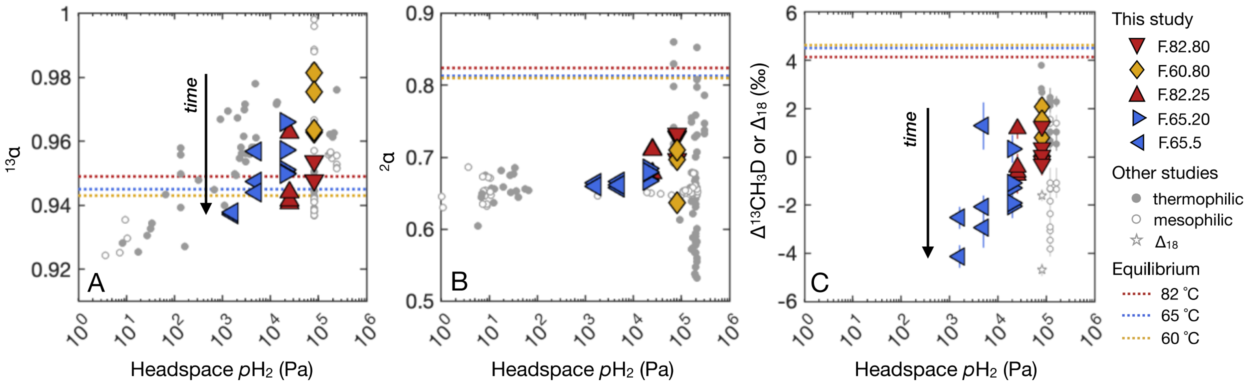

Figure 4

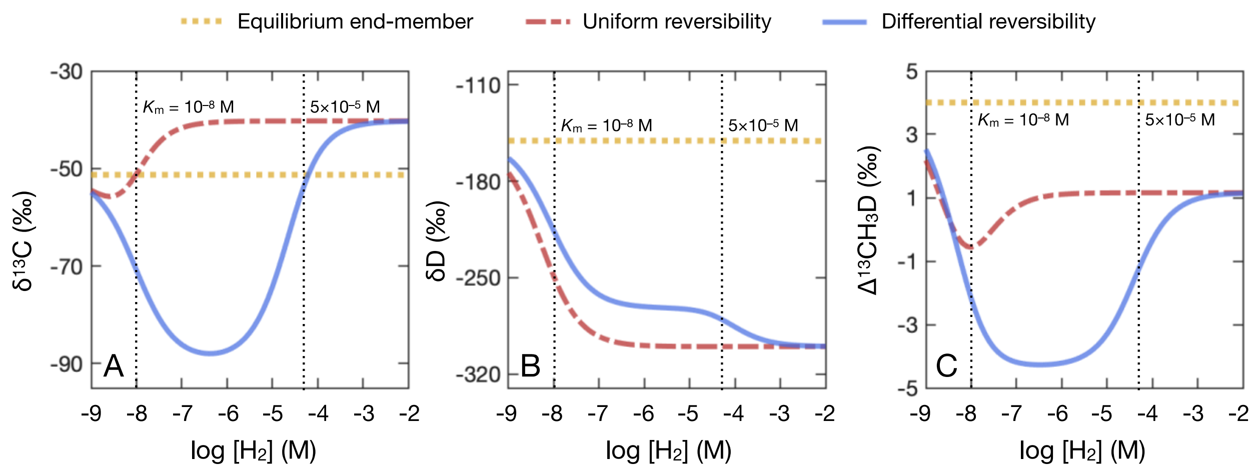

Figure 5

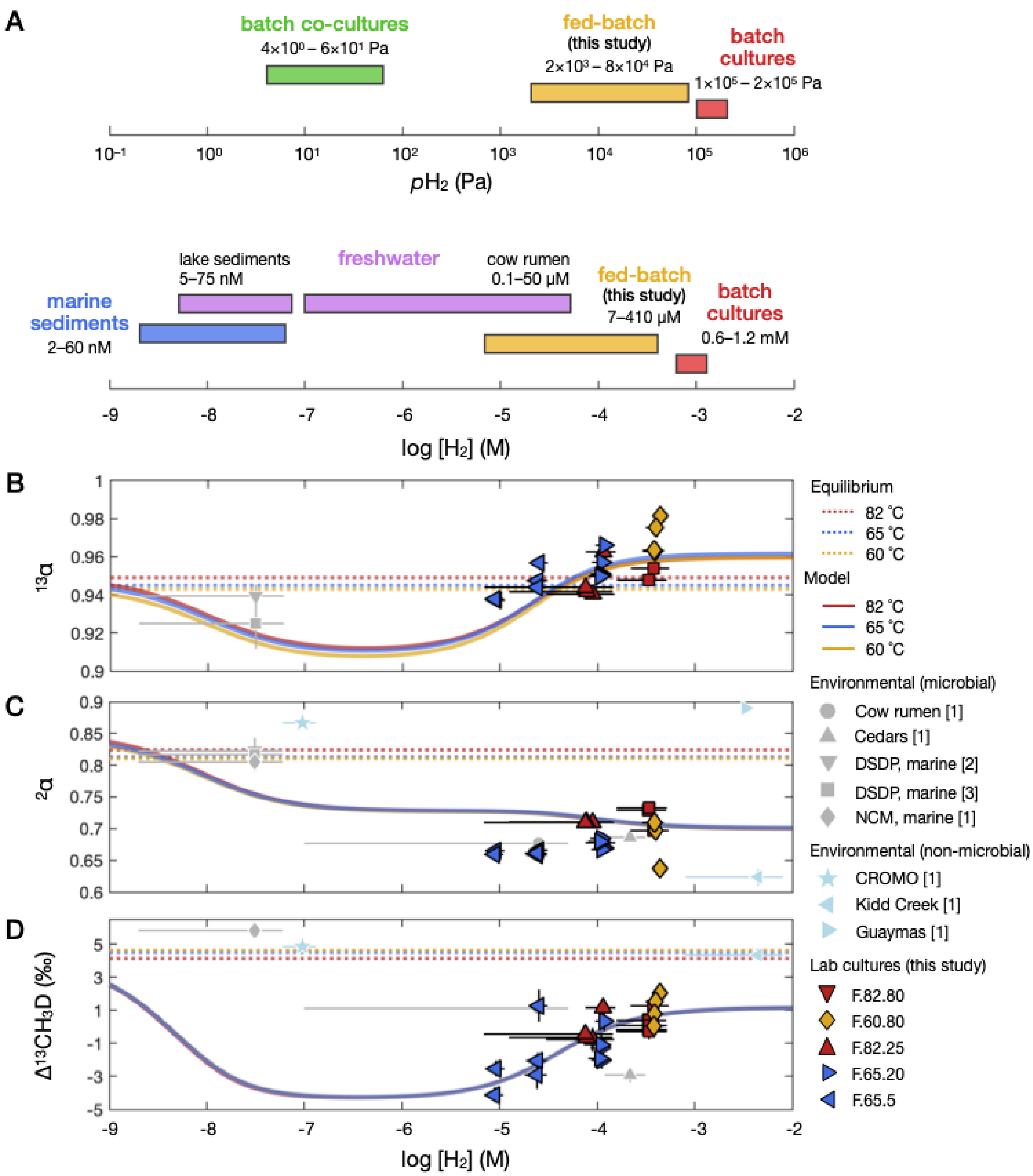

1099

1100 **Figure 6**